Journal of Rock Mechanics and Geotechnical Engineering 18 (2026) 196–213

Contents lists available at ScienceDirect

Journal of Rock Mechanics and Geotechnical Engineering

journal homepage: www.jrmge.cn

Full Length Article

Rock strength assessment in tectonically deformed calcareous rocks integrating equotip, ultrasound velocity, and geo-structural fracture analysis

Elisa Mammoliti [a], Danica Jablonská [b,*], Antonio Ferretti [c], Michele Morici [d], Stefano Mazzoli [a], Mirko Francioni [e]

[a] Dipartimento di Scienze e Ingegneria della Materia dell'Ambiente ed Urbanistica (SIMAU), Università Politecnica delle Marche, Ancona, 60131, Italy
[b] Scuola di Scienze e Tecnologie, Sezione di Geologia, Università di Camerino, Camerino, 62032, Italy
[c] Geotechnical Engineering Services Ltd, Ancona, 60131, Italy
[d] School of Architecture and Design (SAAD), University of Camerino, Ascoli Piceno, 63100, Italy
[e] Dipartimento di Scienze Pure ed Applicate, Università degli Studi di Urbino Carlo Bo, Urbino, 61029, Italy

ARTICLE INFO

Article history:
Received 30 December 2024
Received in revised form
31 May 2025
Accepted 2 June 2025
Available online 17 July 2025

Keywords:
Non-destructive testing
Uniaxial compressive strength
Equotip
Ultrasound pulse velocity
Fracturing
Calcareous rocks

ABSTRACT

In complex geological environments, the analysis of drill cores to determine rock strength can be challenging due to the wide variability in the degree of fracturing, leading to subjectivity in the collection of representative samples for uniaxial compressive strength testing. This study evaluates non-destructive techniques on calcareous rocks with different tectonic deformations, including Equotip hardness, ultrasound P-wave velocity, thin section analysis, and calcimetry, integrated with photogrammetric fracture analysis. The investigated carbonate rock samples are sourced from drill cores derived from the Umbria-Marche fold and thrust belt (northern Apennines, Italy), including a gently dipping limb of an anticline, a hinge zone of an anticline, and a fault zone associated with a thrust. Fracture intensity, quantified by the *P*21 parameter using photogrammetric techniques on pre-loading rock samples, is assessed alongside macroscopic identification of discontinuities (such as stylolites, veins, and joints) using marker colours to monitor failures during uniaxial compression testing. Empirical correlations depicted by single and multi-linear relationships indicate a strong dependence between the mechanical and physical properties of limestones. Both Equotip and P-wave velocity are influenced by fracture intensity, but P-wave velocity varies significantly with discontinuity orientation, especially at 45°–90°. To refine uniaxial compressive strength predictions and mitigate multicollinearity, statistical approaches, including linear and multilinear regression, Principal Component Analysis and Gaussian Process Regression, were tested. Findings improve the reliability of non-destructive techniques for assessing rock strength in structurally complex settings, with implications for geotechnical applications.

1. Introduction

Tectonic deformation and stresses that rocks experience over geologic time result in the formation of sets of discontinuities, ranging from micro- and meso-cracks to large faults, joints, veins, stylolites, and others (Baud et al., 2014; Cilona et al., 2014). These discontinuities strongly influence rock mechanical behaviour, affecting parameters such as strength, failure modes, and crack propagation. Their role is particularly critical in engineering geology applications, including slope stability, tunnelling, mining, and reservoir development (Barton, 1973; Bieniawski, 1973; Brideau et al., 2009). Fracture sets can form either as part of a unified deformation event, exhibiting interconnected kinematics and mechanics, or through a series of events under varying boundary conditions (Toussaint et al., 2018). This complexity contributes to rock anisotropy, significantly impacting the

* Corresponding author.
E-mail address: danica.jablonska@unicam.it (D. Jablonská).
Peer review under responsibility of Institute of Rock and Soil Mechanics, Chinese Academy of Sciences.

https://doi.org/10.1016/j.jrmge.2025.06.012

compressive and tensile strength of rocks (Einstein and Dershowitz, 1990; Bewick et al., 2015; Zuo et al., 2020) and the velocity of elastic waves. The mechanical properties, crack propagation paths, and macro-failure modes are influenced by various characteristics of the flaws, including their shape, number, length, and orientation with respect to the applied load. Fracture orientation plays a fundamental role in rock strength, as it controls both the initiation and propagation of cracks under stress and determines distinct failure modes (Wang et al., 2019; Wong, 2013; Hoek and Martin, 2014; Sarfarazi and Haeri, 2016; Cao et al., 2019; Zhang, 2020; Zhao et al., 2023). At low angles, pre-existing fractures tend to favor shear failure along discontinuity planes, whereas at higher angles, failure transitions to a combination of axial splitting and tensile fracturing (Zhang, 2020; Zhao et al., 2023). In this regard, limestone formations are highly brittle and often exhibit complex fracture distributions due to their diagenetic history and tectonic deformation (Baud et al., 2016; Zuo et al., 2020). Their brittle nature, combined with a complex diagenetic history, frequently results in the formation of stylolites and veins, which can significantly influence mechanical behavior and failure patterns by acting as preferential failure planes (Baud et al., 2016). While numerous studies have investigated the impact of fracture orientation on rock strength in various lithologies, such as sandstones (Aliabdo, 2012; Askaripour et al., 2022; Brady and Brown, 2006; Brozovsky, 2014), granite (Lee and Jeon, 2011; Morgan et al., 2013), marble (Wong and Einstein, 2009) and gypsum (Wong and Einstein, 2009; Park and Bobet, 2010), research specifically focused on limestones remains more limited (Wang et al., 2019; Baud et al., 2016; Cao et al., 2019). Traditional uniaxial compressive strength (UCS) tests are widely used to assess rock strength, but their applicability is limited in fractured rocks due to sample preparation constraints and the high variability of results. Given the complexity of fracture networks and their direct impact on mechanical strength, Non-Destructive Testing techniques have become increasingly important for evaluating fractured rocks. These methods provide a cost-effective alternative to UCS tests, which require specific specimen dimensions and can be destructive (Sbartaï et al., 2012; Theodoridou et al., 2015; Azimian, 2017; Yilmaz and Goktan, 2019; Aldeeky et al., 2020). Among these methods, rebound-based devices such as the Schmidt hammer and Equotip (EQ) have been widely used in engineering geology. These devices measure the rebound or deceleration of a spring-loaded mass impacting the surface of a sample (Aydin and Basu, 2005). The Schmidt hammer, though widely used, can damage rock surfaces due to its high impact energy, limiting its applications. Recent developments (Kawasaki et al., 2002; Kompatscher, 2004; Aoki and Matsukura, 2008; Coombes et al., 2013; Mammoliti et al., 2021) have introduced the EQ as a viable alternative. The EQ uses a smaller impact body (3 mm diameter tip) and applies lower impact energy (11.5 Nmm for a D-probe), making it a less damaging and more precise method for characterizing rock surface hardness (Mammoliti et al., 2021, 2024). Despite the increasing use of EQ in rock mechanics, the influence of fracture networks on EQ measurements remains poorly understood. While several studies have explored the relationship between Schmidt hammer rebound and fracture intensity (Greco and Sorriso-Valvo, 2005; Poblet et al., 2022), the correlation between EQ rebound and $\sigma_{c,}$ values in fractured limestones is still insufficiently investigated. Unlike previous studies, which primarily focus on the qualitative role of fractures in rock strength, this work establishes a direct, quantitative relationship between the degree of fracturing ($P21$) and σ_c. The $P21$ parameter is defined as the total fracture length per unit area (expressed in m/m^2) (Priest and Hudson, 1976; Gomez-Heras et al., 2020; Tsoutrelis and Exadaktylos, 1993) and in this paper is extracted using photogrammetric techniques, allows for a more objective characterization of fracture intensity, reducing subjectivity in rock strength estimation. Additionally, by distinguishing different geological-structural domains (e.g., anticline hinge, overturned limb, thrust zone), this study enhances the understanding of how tectonic deformation influences rock strength, improving the applicability of non-destructive techniques in complex structural settings.

Mammoliti et al. (2024) demonstrated a strong correlation between EQ and fracture intensity at the site scale, but further research is needed to assess its applicability at the sample scale. In particular, it is not yet clear how fracture intensity and fracture orientation influence the rebound values of EQ, and whether these variations can be systematically integrated into strength prediction models. This study aims to integrate multiple non-destructive methods, including EQ rebound testing, ultrasonic wave velocity, and UCS testing, to evaluate rock strength in fractured limestones. By incorporating fracture intensity analyses and geological-structural characterization, we seek to improve the reliability non-destructive -based strength estimations. Furthermore, we aim to address the challenges of UCS modelling in fractured rocks, which is a key unresolved issue in rock mechanics. Many studies rely on simple or multilinear regression models (Sharma and Singh, 2008), but our findings demonstrate that multicollinearity between fracture parameters significantly affects model stability. To overcome this, we apply Principal Component Analysis and Gaussian Process Regression, which provide more robust predictive models and help account for complex parameter interactions.

2. Geological background

The investigated samples originate from Cretaceous-Eocene basinal limestones of the Umbria-Marche succession, Apennines, Italy (Fig. 1a and b). This region has been shaped by multiple tectonic regimes from the Jurassic to Oligocene, influencing both deposition and structural framework of the area (Fig. 1b). During the Late Triassic to Early Jurassic, a carbonate platform dominated the area (Centamore et al., 1971) until rifting in the late Early Jurassic led to the formation of structural lows, several hundred meters deep, that received thick pelagic and hemipelagic fill; and structural highs with thinner cover (Bernoulli and Jenkyns, 1974). Continuing basinal deposition of pelagic carbonates gradually reduced pre-existing topographic variations. Several lines of evidence suggest that, during the Cretaceous to Oligocene, the region experienced another pulse of extensional tectonics that is testified by dissimilar thickness of the formations throughout the basin (Marchegiani et al., 1999), and distinct structural features (Cello et al., 1997). The end of the Cretaceous to early Paleogene saw facies transition, from the dominant pelagic and hemipelagic deposition forming limestones and marly limestones, with an upward increase in argillaceous content (Fig. 1), to impulses of calcarenite deposition coming from distal platforms and mass transport deposits accumulating in basin depocenters (Colacicchi et al., 1970; Bice et al., 2007). During the Oligocene, a collision between the Adria microplate and Eurasian Plate caused progressive shortening, initiating folding and thrusting from west to east (Deiana and Pialli, 1994; Calamita et al., 1994). This initiated folding and thrusting in the study area. The current extensional regime in the inner Apennines has resulted in a NW-SE striking normal fault network. The samples were collected from the cores drilled in the localities Pontechiaradovo (PC), Gattuccio (GT), Valtreara (VT), San Cristoforo (SC); Casa Meloni (CM) and Rochetta (RC) (Fig. 1a). They comprise limestone, marly limestone and calcareous marls specimens and they are listed in Table 1. These lithofacies occur in different structural settings: (1) a broad anticline characterized by open fractures, often filled with calcite; (2) a

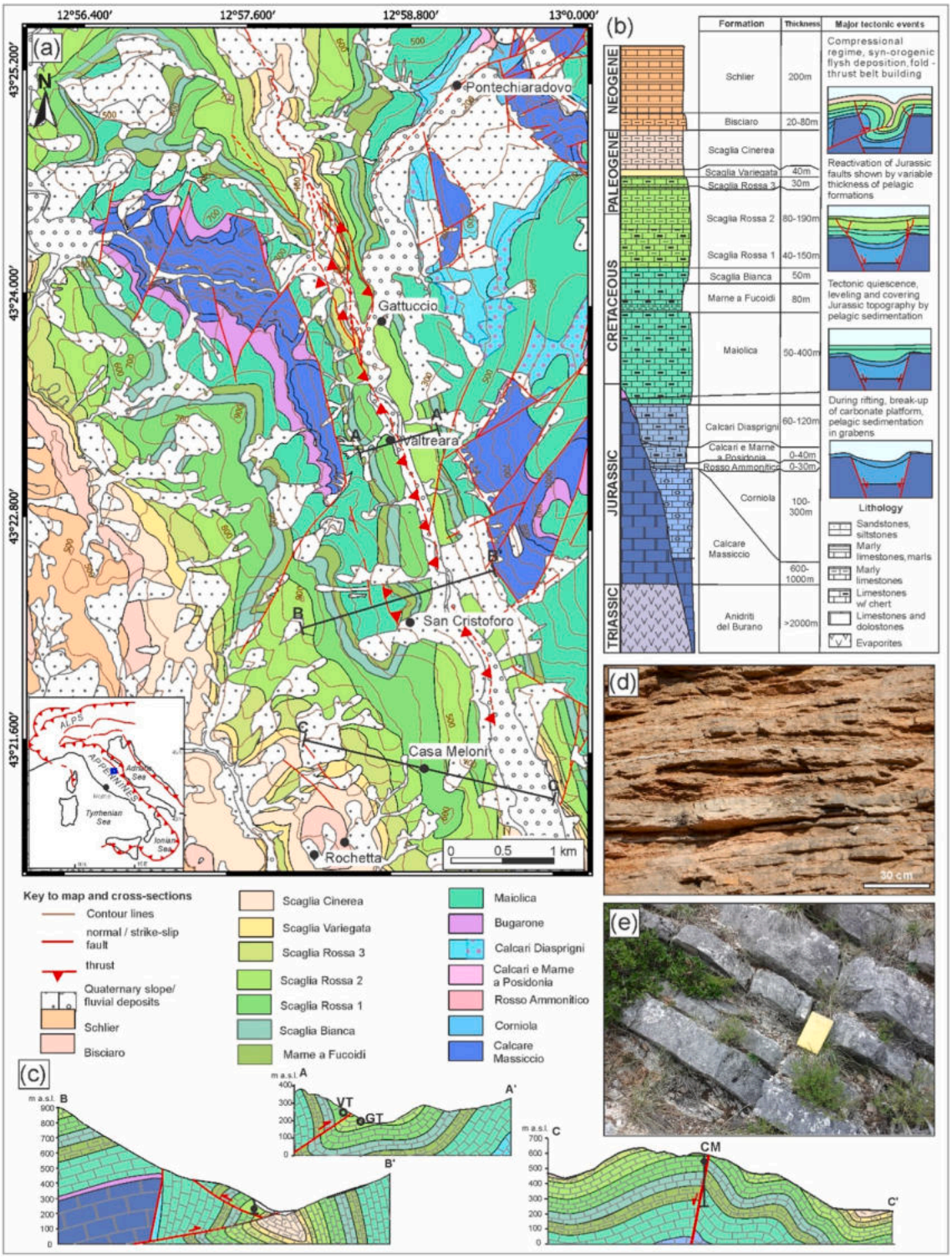

Fig. 1. Geological overview of the area: (a) geological map of the studied area with the position of the rock cores (in bold) and samples name (in italics), (b) Stratigraphic column, not to scale, with the major tectonic events that impacted the studied area, (c) geological cross sections passing same structures as the sampled cores; examples of the lithotype at the outcrop, (d) marly limestone intercalated with argillaceous layers, the upper part of the Scaglia Rossa 3, and (e) calcarenites abundant in the upper part of Scaglia Rossa 2 Fm.

thrust front (and backthrust) where multiple splays and horizons of C-S tectonites are present, destroying the original rock fabric; (3) a blunt syncline with limited deformation; (4) an overturned limb with elevated number of stylolites and fractures; and (5) a very blunt flank of a monocline.

3. Materials and methods

This chapter details the methodologies used to evaluate the relationship between the physico-mechanical properties and fracture intensity of rock samples. Non-destructive techniques,

Table 1
Summary table of the examined stratigraphic units, including lithofacies descriptions, sampled rock types, and corresponding tectonic settings where the samples were collected.

Stratigraphic level	Description of the lithofacies	Sampled lithofacies	Samples taken in the tectonic setting and corresponding sample numbers
Rosso Ammonitico	Intercalation of 5–15 cm pinkish top maroon marly limestones beds with layers of red mudstones	Maroon marly limestone	blunt flank of a monocline 9B (PC)
Maiolica	Cherty micritic limestones of 10–35 cm thick beds, often hosting nodules of pyrite	White micritic limestone	hinge of an anticline 6A (CM), back thrust 8A,9A (SC)
Scaglia Rossa	(2nd and 3rd member) Second member comprises thin-to thick-bedded pinkish limestones often intercalated with calcarenites and calcirudites that are recrystalized with thin marlstone or shale partings. The 3rd, marly member comprises of interbedded (5–15 cm thick) marlstones and shales and is commonly slumped.	Pinkish marly limestone	Overturned limb 2A,2B; (SC) hinge of syncline 4A, 4B (GT)
		Calcarenite and recrystallized calcarenite	hinge of an anticline 5A (CM),
		Light pink to brown marly limestone	Thrust zone 3A, 3B (VT)
Bisciaro	Intercalations of grey to brown marly limestones (10–50 cm) and calcareous marls (10–30 cm), volcanic tuffs often present as thin layers	Greyish-brown marly limestone	Broad syncline 7A, 10A (RC)

such as EQ hardness testing (a mechanical property) and ultrasonic P-wave velocity measurements (a physical property), are highlighted for their effectiveness in predicting σ_c of fractured rocks. The calcimetric analysis, conducted to determine carbonate content (physical property), is used to support the data analysis. Linear and multiple regression analyses are employed to develop predictive models, with multiple regression providing a more accurate representation of the variation in σ_c.

3.1. Sample preparation

Multiple cylindrical rock samples were obtained from borehole cores extracted in different structural settings, including the hinge of a blunt anticline, the hinge of a meso-scale anticline, and thrust sheets (Fig. 1). Borehole core samples were preferentially selected to mitigate the effects of weathering and dilation commonly observed in outcrop environments. Material for calcimetry analysis (total carbonate content) and thin section preparation was sourced from corresponding sections of the rock, several millimetres above the sample core to ensure consistency with lithology (clay content in limestone) and structural features (stylolites, veins). At the mesoscale, detailed characterization of the rock samples was conducted, encompassing parameters such as dip angle of the bedding, in addition to joints, veins, and stylolites. Cross-cutting relationships were established to elucidate the structural context. It is pertinent to mention that borehole sampling was not oriented with cardinal coordinates; hence, cross-cutting relationships are described relative to bedding. To mitigate the influence of sample size on experimental outcomes, all samples were standardised to a cylindrical shape following the established sampling standards (Bieniawski and Bernede, 1979; ASTM D2938-79, 1980). Samples were prepared to ensure parallelism of the sample ends within an accuracy of 0.05 mm. To minimise the impact of water saturation on measured properties, samples underwent drying in an oven chamber at 110 °C for 24 h (ASTM D2938-79, 1980). In fact, as reported by several authors (Hawkins and McConnell, 1992; Török and Vásárhelyi, 2010), the water content significantly impacts rock strength, as well as P-wave velocity (Wyllie et al., 1956; Török and Vásárhelyi, 2010) and EQ values (Desarnaud et al., 2019). For each rock core (GT, VT, SC, CM, RC and SC in Fig. 1a and Table 1), at least two rock samples are extracted and designated with an identification code (Fig. 2a). All samples are listed in Table 2.

3.2. Calcimetric analysis

Calcimetric analysis was employed using the De Astis calcimeter (Correns, 1968) set at a temperature of 20 °C, to determine the calcium carbonate content. These analyses were conducted at the Stratigraphy, Sedimentology, and Paleoecology Laboratory of the Università Politecnica delle Marche (Italy). Representative flakes for calcimetry analysis were selected based on their visual and geological characteristics, focusing on those displaying clear stylolitic planes and associated alteration minerals. Samples were chosen to reflect variability in stylolite development and mineralogy, with flakes of different sizes included. Flakes were carefully dried and ground to a fine powder using a mortar and pestle to ensure homogeneity. Briefly, a known weight of the powdered sample was transferred into a beaker. Next, a measured volume of hydrochloric acid (HCl) was added to dissolve the carbonate minerals present in the sample. The solution was then heated gently until effervescence ceased, indicating complete carbonate dissolution. The quantity of calcium carbonate in the sample is determined based on the calibration equation established at the outset of the test. The calcimetric analysis was conducted on one rock sample from each core in the series, which was deemed representative. For each rock sample, the analysis was performed on three flakes, from which an average calcium carbonate content value was calculated.

3.3. 3D fracture intensity calculation

Photogrammetric techniques were employed to generate high-resolution 3D models of the rock samples, which were then analysed to determine fracture intensity. 3D models were reconstructed from images acquired with a Canon EOS 100D camera with the standard kit lens fixed at 55 mm. Sample images were captured inside a photo lightbox to maintain full control over camera positioning and ambient lighting, minimizing shadows and glare to ensure high image quality. To achieve the desired >70% inter-photo overlap, fracture samples were placed on a 360° rotating stage and manually rotated in 10° increments between

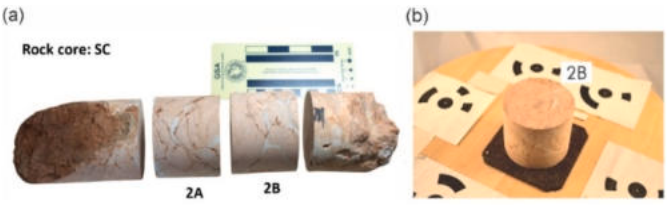

Fig. 2. (a) Example of rock sample preparation from a single rock core, and (b) Photogrammetric setup with reference markers for 3D rock sample reconstruction.

Table 2
Summary of the samples examined with indication of the core depth, sample diameter and height/diameter ratio.

Rock core	Depth (m)	Rock sample	Diameter (cm)	Height/Diameter ratio
SC	57.5	1A	7.5	1
		1B	7.5	1
		1C	7.5	1
SC	58.5	2A	7.5	0.87
		2B	7.5	0.87
VT	28	3A	7.5	1.07
		3B	7.5	1
GT	21.7	4A	7.5	1
		4B	7.8	0.96
CM	26.4	5A	8.5	1.06
		5B	8.5	1.06
CM	247	6A	6	1.17
RC	22	7A	10.5	0.95
CM	28	8A	6.5	1
SC	105	9A	6	1.17
	105	9B	8	0.88
RC	28	10A	5.5	1

shots (Fig. 2b). Photographs were taken at a fixed camera-to-object distance of 45 cm, using three distinct angles: horizontal (0°), oblique (50°), and perpendicular to the cut surface. For the horizontal and oblique angles, images were captured every 10° azimuthally around the sample to ensure full 360° coverage. Image processing was conducted using Metashape software (Agisoft, 2020), with calibration procedures to correct lens distortions and align multiple reconstructions for accuracy. These steps ensured the precise identification of fracture traces and minimized potential measurement errors. The 3D models provided a detailed representation of the rock surfaces, which were manually extracted using CloudCompare software (Girardeau-Montaut, 2016). The areal fracture intensity parameter (*P*21, Dershowitz and Herda, 1992), which is defined as the length of fracture traces per unit area (L-1) was calculated for each sample considering joints, calcite-filled veins, and stylolites. Additionally, the angle of inclination of each fracture surface relative to the vertical load and ultrasonic pulse wave direction was determined to understand the orientation effects on rock strength.

3.4. Non-destructive testing

3.4.1. Equotip hardness tester

The EQ hardness tester was employed to non-destructively assess the hardness of the rock samples, quantified as the Leeb rebound number (*L*). Manufactured by Proceq (1977), EQ is a rebound-based device that has gained increasing utilisation in engineering geology over recent decades (Verwaal and Mulder, 1993; Kawasaki et al., 2002; Aoki and Matsukura, 2008; Mammoliti et al., 2024). It offers several advantages over comparable instruments, such as the Schmidt hammer and needle penetrometer, such as a wide range of impact energy, covering a wide range of rock materials, from extremely weak and weathered to very strong rocks. EQ impacts are derived from a 3 mm spherical tip, enabling minimally destructive rebound hardness tests Proceq (1977). For these reasons, EQ has demonstrated superior reliability compared to the Schmidt hammer for estimating σ_c (Kovler et al., 2018; Mammoliti et al., 2021, 2024). To evaluate the potential of EQ in assessing the rock strength of samples with varying fracture intensity from complex geological environments (characterized by significant tectonic disturbance), rebound data were systematically acquired for each analysed sample. To ensure statistical robustness, nine measurement points (indicated by red points in Fig. 3b) were evenly distributed on both the lateral surfaces and bases of the cylindrical samples. At each measurement point, forty repeated impacts were performed using the repeated impact measurement approach as described by Mammoliti et al. (2024). The data collected from these impacts were then averaged to determine the mean Leeb rebound number ($EQ\,L_{mean}$), serving as a representative value for each analysed sample.

3.4.2. Ultrasonic P-wave velocity

Ultrasonic testing is a non-destructive method used to qualitatively assess the presence or absence of internal discontinuities within materials, such as fracture planes and inhomogeneities (Kahraman, 2001). This technique relies on certain relationships linking the speed of elastic wave propagation within a material medium to its elastic properties. The equipment used is a NOVA-SONIC digital ultrasound detector equipped with two probes—one transmitting and one receiving—at a frequency of 55 kHz, positioned at flat cuts through the core axis of the cylinder specimen (Fig. 3a). The wave velocity of the rock sample was measured in accordance with the ASTM standards (ASTM D2845-05, 2005), and acoustic waves were recorded at regular force intervals (5 kN in this test, approximately 10 s). Following the test, P-wave velocities of the rock samples under different pressures were calculated. Prior to testing, the surfaces of each element underwent sanding to ensure sufficient smoothness and removal of dust. Probes were coupled to the structure using specific ultrasonic gel to facilitate a suitable interface surface for accurate transmission and reception of ultrasonic waves. The tests were conducted using the direct method, positioning the probes so that the shortest path of the waves traversed the section of the element. For each sample, five readings were collected, or enough readings to ensure stability in the travelling time for at least three successive readings. A typical diagram of the test procedure is illustrated in Fig. 3a. This test is instrumental in understanding the effects of micro-fracturing on the physical and mechanical properties of rocks. Factors such as pores and micropores, joints and calcite veins, anisotropy as well as texture and mineralogical composition, influence the P-wave velocity. Additionally, lithology, weathering, alteration zones, bedding planes, and joint properties (such as filling material, water presence, dip, and strike) play significant roles in sound velocity determination.

3.4.3. Uniaxial compressive strength

In this study, the rock strength was evaluated in the laboratory by conducting UCS tests on the samples properly prepared as described in paragraph 3.1. A hydraulic press (maximum load equal to 400 kN) was used to axially load each specimen in the

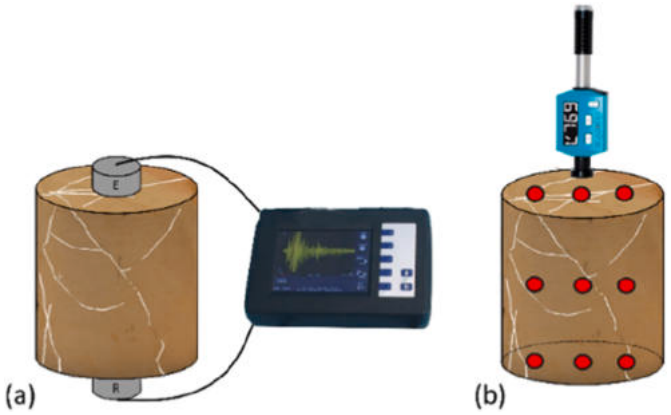

Fig. 3. (a) Overview of the ultrasound P-wave velocity test, and (b) EQ hardness testing with indication of the EQ measuring points (points).

absence of any confining pressure. The load was progressively applied by imposing a constant vertical displacement rate of 2 mm/min until the breakdown condition was reached. This latter was identified in the displacement-load curve by the occurrence of a peak followed by a noticeable drop. Such maximum load was then divided by the cross-section area of the sample to obtain the σ_c value. As extensively documented in the literature (Hawkins, 1998; Mogi, 2006; Tuncay and Hasancebi, 2009; Li, 2021), a specimen height-to-diameter ratio (H/D) equal to or greater than 2 is required to obtain reliable test results. Since the H/D ratio in this study ranges from 0.87 to 1.17, the formula is applied to convert the measured σ_c value of specimens with an H/D ratio less than 2 to the σ_c* of a specimen with a standard ratio of 2:

$$\sigma_c^* = \sigma_c \Big/ \left(0.88 + 0.24\frac{D}{H}\right) \quad (1)$$

3.5. Regression analyses

Regression analysis serves as a statistical method for forecasting a dependent variable by examining changes in one or more independent variables. In the fields of rock engineering and engineering geology, regression analysis is used to develop predictive models concerning pertinent rock properties. In this context, regression analysis is essential for understanding and predicting complex relationships between measurable rock properties and their engineering behavior. This investigation conducted both simple and multiple regression analyses to formulate predictive models for the σ_c of calcareous rocks using three variables: V_p, EQ L_{mean} and $P21$. These variables were selected based on their established significance in influencing rock strength and their ease of measurement in both field and laboratory settings. Linear and multiple linear regressions were employed in this study due to their proven effectiveness in rock mechanics literature for modelling relationships between rock properties and strength parameters. It must be highlighted that different interpolation methods have been tested in this study and the linear regression analyses resulted in being the most suitable. Previous studies have demonstrated that linear models can provide a reasonable approximation of the relationships between σ_c and independent variables in many types of rocks, making them a suitable choice for initial predictive modelling (Kawasaki et al., 2002; Aoki and Matsukura, 2008). Multiple linear regression allows for the simultaneous consideration of several influencing factors, providing a more comprehensive understanding of how these variables interact to affect rock strength. The Pearson correlation coefficient (r), the coefficient of determination (R^2), and the p-value to evaluate the strength and significance of the relationships. Collinearity among predictors was assessed using Variance

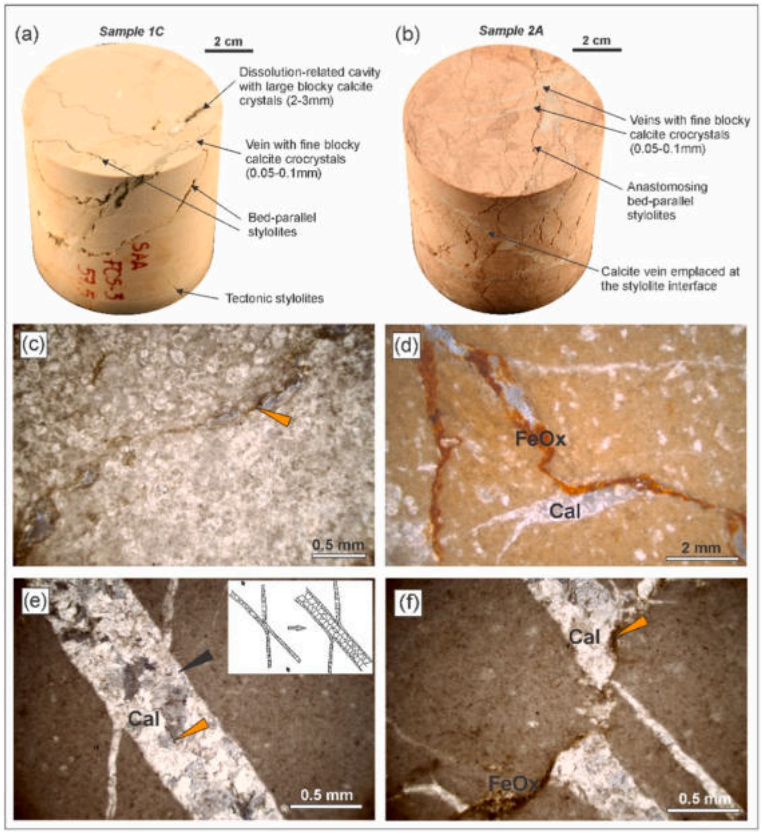

Fig. 4. Hand specimens and microphotographs of the sampled rocks: (a) Sample 1C: Example of crystalline limestone specimen with bed-parallel stylolites, veins and dissolution cavities, (b) Sample 2A: Example of pink marly limestone specimen and its structural features, (c) Sample 1A: thin bed-parallel stylolite separating fossil-dominant grainstone and crystalline carbonate, with reddish material at the interface. The stylolite marks the volume loss through calcite vein which progressive growth towards the centre (small calcite crystals marked by black arrow), (d) Sample 4B showing a stylolite – veins interaction,: partial pressure solution impacts the rock and the vein in the lower part; the vein in the upper part of the picture may have been used the sylolite surface for propagation, (e) microcrystalline limestone (Sample 5A) with two sets of veins; both veins initiated as coeval fractures, after opening filled with fine blocky calcite crystals, the larger syntaxial vein was later re-opened and filled by larger blocky crystals coarsening towards the centre (orange arrow), and (f) Sample 5A, Two sets of veins cross-cut by tectonic stylolites resulting in volume loss. The stylolite interface is filled with argillaceous material and pyrite grains (orange arrow). Cal = calcite; FeOx = iron oxides.

Inflation Factors (VIFs). Due to significant multicollinearity, Principal Component Analysis (PCA) was applied to refine the models by reducing dimensionality and collinearity. Model performance was evaluated based on R-squared, Root Mean Squared Error (RMSE), and p-values for statistical significance. In this analysis, we applied Bayesian Gaussian Process Regression (GPR), a powerful non-parametric machine learning technique that models the relationship between predictors and the target variable by considering uncertainty in the data and predictions. The model was fitted using a squared exponential kernel and validated using 5-fold cross-validation to assess its robustness and avoid overfitting. The data includes interactions between predictors to capture complex relationships. The GPR model was implemented in MATLAB using the *"fitrgp"* function. GPR offers several advantages over traditional linear regression. It is a non-parametric method that models complex, nonlinear relationships between variables without assuming a fixed functional form. GPR also quantifies uncertainty in predictions, providing confidence intervals, which is valuable in uncertain data. Unlike linear regression, it handles multicollinearity effectively and captures interactions between predictors, allowing for more flexible and accurate models. Additionally, GPR, when combined with cross-validation, is less prone to overfitting, ensuring better generalization to new data.

4. Results

4.1. Geological and statistical analysis of destructive and non-destructive test results

The examined rock samples were collected from thin-bedded limestones and marly limestones, classified as mudstones, packstones, grainstones, and crystalline and sucrosic limestones (after Dunham, 1962). Since the sample sets come from different structural settings (Table 1) and represent various basin lithotypes, a variety of sedimentary and structural features can be observed. The first set of rock samples (1A, 1B, 1C), from Scaglia Rossa 2, were extracted from a calcarenite bed with a dip angle of ≈60° (overturned fold limb). The calcarenite is crosscut by an array of bed-parallel stylolites, tectonic stylolites (at a high angle to bedding), and calcite-filled veins (Fig. 4a). Thin section analysis revealed that the calcarenite bed was only partially recrystallized (Fig. 4c), likely during burial. Some veins show signs of previous dissolution, containing voids and later inward growth of elongate blocky calcite large crystals (1 mm size), most probably of meteoric origin (Fig. 4a). Samples 2A and 2B were collected from the same location and stratigraphic unit (Scaglia Rossa 2). These samples, consisting of pinkish marly limestone (wackestone), contain a plethora of planktonic foraminifera. Notably, these limestones feature a network of anastomosing bed-parallel stylolites associated with the burial phase.

The array of veins includes structures that developed either along stylolite surfaces or perpendicular to them (Fig. 4b). Some veins abut on the stylolite surface; some are cross-cut by stylolites with apparent offset indicating volume loss; and some veins crosscut the stylolites. These relationships suggest continuous, roughly coeval processes of vein formation and stylolite reactivation and accentuation due to bed rotation within a general framework of continued regional horizontal shortening. The calcite veins contain blocky crystals 0.05–0.1 mm in size. Samples 2A and 2B, which were spaced 1.5 m apart vertically, experienced identical tectonic deformation. However, there are notable differences in the number and types of structural discontinuities between these two samples. This indicates that the geological composition (lithology) plays a crucial role in the mechanical properties of the rock during tectonic deformation. From the point of view of EQ hardness (Fig. 5 and Table 3), these samples exhibit mean values (*EQ* L_{mean}) ranging from 658 L to 731 L, indicating consistent hardness. The minimum values (*EQ* L_{min}) vary significantly, from 305 L to 596 L, while the maximum (*EQ* L_{max}) is consistently high, between 773 L and 840 L.

The standard deviation (*EQ* $L_{st.dev}$) in the SC rock core ranges from moderate to high, indicating some variability within each sample. The σ_c values for these samples range from 30.8 MPa to 51.7 MPa, suggesting strong rock material. The *P*21 values vary, with samples 1A, 1B, and 1C having lower values (0.23–0.36 m/m^2), indicating minimal fracturing, while samples 2A and 2B have higher values (1.07–1.41 m/m^2), indicating increased fracturing. The failure mode for these samples is a combination of intact rock

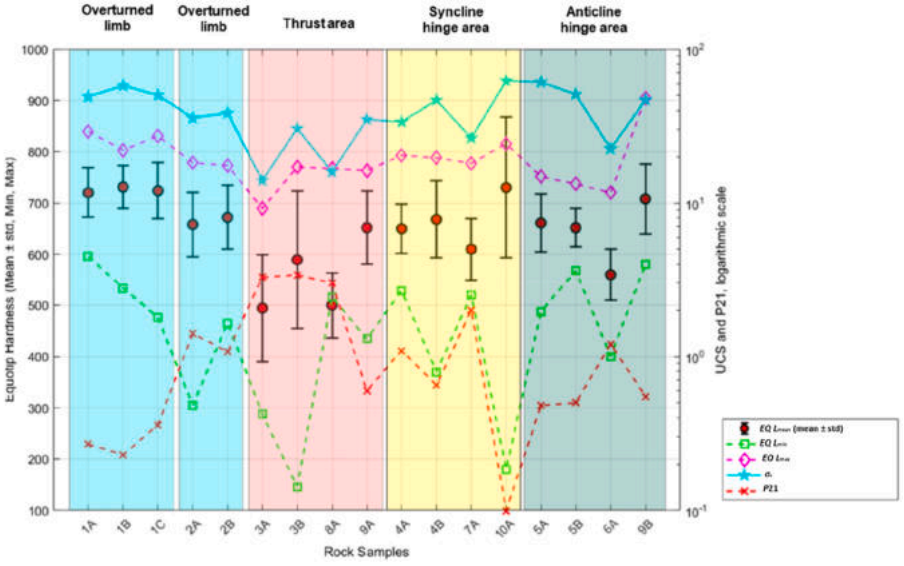

Fig. 5. Comparison of EQ hardness (mean ± std, min, max), σ_c, and *P*21 values across various rock samples; EQ hardness is shown on the primary y-axis, while σ_c and *P*21 are presented on a logarithmic secondary y-axis.

Table 3
Summary of the mechanical parameters derived from σ_c, EQ and ultrasound-pulse velocity tests. *P*21 and failure modes are shown.

Rock core	Rock sample	σ_c (MPa)	*EQ* L_{mean}	*EQ* L_{min}	*EQ* L_{max}	*EQ* $L_{st.\ dev.}$	V_p (m/s)	*P*21 (m/m^2)	Failure mode
SC	1A	43.9	720	596	840	48	5342	0.27	Combination of intact rock and pre-existing discontinuities
	1B	51.7	731	533	803	42	5621	0.23	Combination of intact rock and pre-existing discontinuities
	1C	44.9	724	476	831	54	5646	0.36	Combination of intact rock and pre-existing discontinuities
SC	2A	30.8	658	305	778	63	4244	1.41	Combination of intact rock and pre-existing discontinuities
	2B	33.2	672	465	773	62	4718	1.07	Combination of intact rock and pre-existing discontinuities
VT	3A	12.7	494	288	689	105	926	3.27	Shear failure
	3B	27.3	589	146	770	135	4133	3.4	Shear failure
GT	4A	30.1	650	528	793	48	2564	1.09	Axial splitting
	4B	41.3	668	370	788	75	3535	0.65	Axial splitting
CM	5A	55.1	661	487	751	56	5342	0.48	Axial splitting
	5B	46	652	568	737	38	5386	0.5	Axial splitting
CM	6A	8.5	550	522	812	49	1300	3.4	Combination of intact rock and pre-existing discontinuities
RC	7A	26.4	610	520	777	60	1560	2	Axial splitting
CM	8A	15.9	500	516	767	64	941	3	Axial splitting
SC	9A	34.9	652	434	763	72	5110	0.6	Axial splitting
	9B	46.7	708	580	904	68	4521	0.55	Axial splitting
RC	10A	62.2	730	180	816	137	4300	0.1	Axial splitting

and pre-existing discontinuities. Samples 3A and 3B were collected near a thrust zone (Fig. 1). This marly limestone is highly foliated due to localized deformation within the thrust zone. The foliation surfaces are evident due to the passive accumulation of non-soluble minerals (up to 18%; Table 3) forming parallel planes.

Along these foliation planes, 0.5–3 mm calcite veins developed. Calcite veins are either parallel to the foliation or at 15°. Samples 3A and 3B from rock core VT show significantly lower *EQ* L_{mean} values of 494 L and 589 L, respectively (Fig. 5 and Table 3). The *EQ* L_{min} values are very low, particularly for sample 3B (146 L). The *EQ* L_{max} values are variable, with 689 L for 3A and 770 L for 3B. This group has the highest standard deviation, indicating highly variable hardness. The σ_c values are 12.7 MPa for 3A and 27.3 MPa for 3B. These samples are characterized by high *P*21 values of 3.27 and 3.4 m/m^2, indicating a high degree of fracturing due to tectonic foliation. The failure mode for these samples is shear failure. Samples 4A and 4B were collected in a syncline area and are lithologically similar to samples 2A and 2B, consisting of pinkish marly limestone rich in planktonic foraminifera. The dip angle of the bedding in this core changes frequently due to intense deformation, the dip angle of the sample examined is 15°. The limestone is cross-cut by three sets of stylolites – parallel to the bedding, at 45° and 80° respectively to the bedding. Both bed-parallel stylolites and tectonic stylolites are filled with reddish non-soluble material. The calcite veins either abut the bed-parallel stylolites (Fig. 4d) or are cross-cut by the tectonic ones. In some cases, the veins follow the stylolite surfaces. Cavities up to 5 mm, partially filled with blocky calcite cement, indicate previous dissolution caused by aggressive fluids passing along pre-existing discontinuities. Several sets of calcite veins were observed with cross-cutting relationships. Calcite veins, 60° to bedding, postdate a set of anastomosing stylolites. The stylolite set at a high angle (80°) postdates the veins (Fig. 4c and d). Rusty argillic material is present on all stylolitic surfaces, but the bed-parallel set has the thickest portion, suggesting that the predominant loss of calcite material occurred during the overburden. Veins show several reopening events. Some of these reopened veins are filled with rusty argillaceous material. These samples have *EQ* L_{mean} values of 650 and 668, with *EQ* L_{min} values of 528 and 370, respectively. The *EQ* L_{max} values are 793 for 4A and 788 for 4B. *EQ* $L_{st.dev.}$ is moderate, indicating some variability in hardness. The σ_c values are 30.1 and 41.3 MPa, respectively. The *P*21 values are 1.09 and 0.65, indicating moderate fracturing. The failure mode for these samples is axial splitting. Samples 5A and 5B were collected from the hinge area of a large anticline. The high dip angle (45°–55°) of the beds suggests that the sampling area is likely in the inner-arc zones with localized compression. Like samples 1A and 1B (Fig. 4c), these specimens represent calcarenites from the Scaglia Rossa 2. However, unlike the previous samples, they are highly recrystallized into very fine crystalline limestone (Fig. 4e and f). Calcite veins and stylolites are scarce. Some calcite veins host two types of calcite cement (Fig. 4e) – fine blocky crystals at the walls and large blocky crystals in the central portion of the veins, suggesting at least two crack-seal events. Bed-parallel stylolites are scarce and cross-cut calcite veins (Fig. 4f). This may, as in the previous case, indicate reactivation of the bed-parallel stylolites due to bed rotation during continuous folding. These samples have *EQ* L_{mean} values of 661 and 652, with *EQ* L_{min} values of 487 and 568, respectively (Fig. 5 and Table 3). The *EQ* L_{max} values are 751 and 737, with moderate standard deviations indicating some variability in hardness. The σ_c values are 55.1 MPa for 5A and 46.0 MPa for 5B. The *P*21 values are low, at 0.48 m/m^2 and 0.5 m/m^2, indicating minimal fracturing. The failure mode for these samples is axial splitting. In summary, the analysis reveals that the EQ hardness data (*EQ* L_{mean}, *EQ* L_{min}, *EQ* L_{max}, and *EQ* $L_{st.dev}$) and σ_c values are inversely related to *P*21 values, particularly evident in samples 3A and 3B, which has the highest *P*21 values and the lowest σ_c and EQ values. This suggests that samples with higher fracture intensity (higher *P*21) tend to have lower σ_c and more variable hardness, highlighting the impact of tectonic foliation and fracturing on rock strength and hardness. The sample set 3A and 3B are derived from rock core VT, respectively located in the deformation zone of a thrust sheet (Fig. 1). From a geological perspective, these sample are beige marly limestones belonging to the upper part of the 2nd member of Scaglia Rossa Fm., and characterised by tectonic foliation, represented by planes of marly limestone and claystone invaded by calcite veins. The bedding dip angle is 55–60°, and the foliation may have caused overall overprinting of the structures. Sample 6A is a micritic limestone (Maiolica Fm.) coming from the hinge area of a large anticline. The high dip angle (45°–55°) of the beds suggests that the sampling area is likely in the inner-arc zones with localized compression. The sample contains bed-parallel stylolites, calcite veins, and shear fractures. There are at least 2 sets of veins, as one set predates and one post-dates the formation of stylolites. The σ_c of sample 6A is 8.5 MPa, which is the lowest of the dataset. The *EQ* L_{mean} is 550 L, with a V_p of 1300 m/s, and a *P*21 value of 3.40 m/m^2, which suggests a rock that is relatively brittle and prone to shear failure. Samples 7A and 10A represent greyish-brownish marls to marly limestone coming from cores passing a blunt syncline. Both specimens show bed-

Table 4
Correlation matrix (r) of the independent variables $P21$, σ_c, $EQ\ L_{mean}$, V_p.

Variables	$P21$ (m/m^2)	σ_c (MPa)	$EQ\ L_{mean}$	V_p (m/s)
$P21$ (m/m^2)	1			
σ_c (MPa)	−0.89	1		
$EQ\ L_{mean}$	−0.91	0.87	1	
V_p (m/s)	−0.79	0.81	0.84	1

parallel lamination, a high number of microfossils, and no particular structural features (veins, fractures, and stylolites). The dip angle is 20° for sample 7A and 10° for sample 10A. The σ_c values are 26.4 MPa for 7A and 62.2 MPa for 10A, with $EQ\ L_{mean}$ values of 610 MPa and 730 Mpa, respectively. The V_p for sample 7A is 1560 m/s and for sample 10A, it is 4300 m/s. Samples 8A and 9A are specimens of micritic limestone (Maiolica Fm.) extracted from a core passing a back thrust. These samples show a high number of fractures and veins cross-cutting the rock sample. Bed-parallel stylolites contain rusty and greenish clay, and the shear fractures are stylolite-bound, with a 2–5 mm throw. Some of the fractures show cavities formed by dissolution and later partially filled by drusy calcite. The σ_c for 8A is 15.9 MPa, with a $EQ\ L_{mean}$ of 500 L and a V_p of 941 m/s. For 9A, the σ_c is 34.9 MPa, with an $EQ\ L_{mean}$ of 652 L and a V_p of 5110 m/s. Sample 9B is marly limestone with maroon-greyish bands of the mudstone/marls. Shear fractures and stylolites are present but are less common. The dip angle corresponds to 22°. The thin section revealed a high fossiliferous content of small bivalves, small ammonites (<3 mm), and filaments. The σ_c for this sample is 46.7 MPa, with a $EQ\ L_{mean}$ of 708 L and a V_p of 4521 m/s. These parameters reveal that the rock samples exhibit varying degrees of strength, brittleness, and structural complexity, which are influenced by their mineralogical composition, the presence of discontinuities, and the structural features in the area. The combination of high fossil content, stylolites, and fractures in the samples suggest complex mechanical behavior influenced by the regional tectonic setting.

4.2. Simple linear regression results

In this study, the correlation coefficient presented in Table 4 indicates a strong relationship between the variables analysed and the correlation matrix ($0.79 < |r| < 0.91$), suggesting that changes in one variable are closely associated with changes in another. In detail, the highest correlation is evidenced for $EQ\ L_{mean}$ vs. $P21$ ($r = -0.91$), evidencing that fracture intensity plays a fundamental role in the strength of rock samples. The lowest is for V_p vs. $P21$. σ_c values are strictly influenced by both fracture intensity $P21$ ($r = -0.89$), $EQ\ L_{mean}$ ($r = 0.87$). The scatter plots depicting the relationships among the examined variables are showcased in Fig. 6, accompanied by their corresponding equations, correlation coefficient (r), and coefficient of determination (R^2).

4.3. Multilinear regression and principal component analysis results

This chapter presents a comprehensive analysis of multilinear regression models applied to our dataset, complemented by Principal Component Analysis (PCA) to address potential multicollinearity issues. The primary aim is to evaluate the relationships between σ_c and various predictor variables, including $EQ\ L_{mean}$, V_p, and $P21$, and their interactions. We begin with an analysis of σ_c based on $EQ\ L_{mean}$ and V_p, applying a multiple linear regression

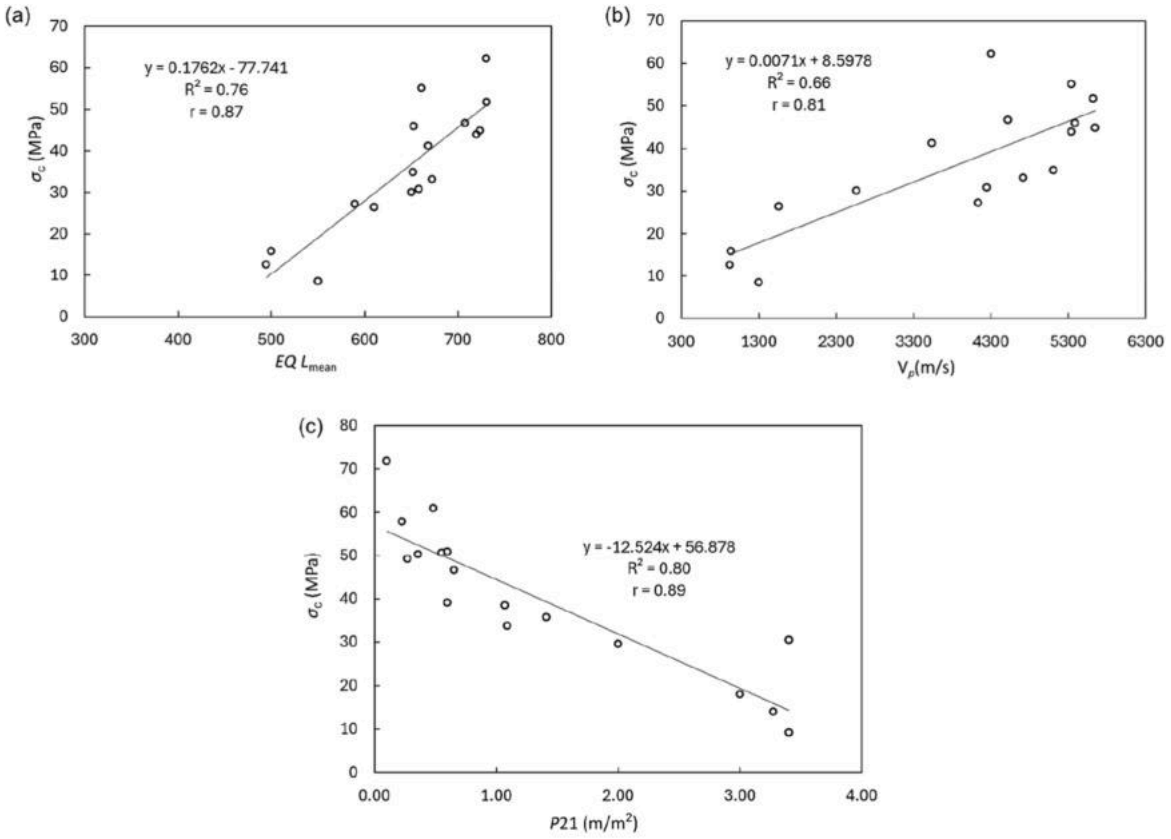

Fig. 6. Scatter plots showing the relationships of: (a) $EQ\ L_{mean}$ vs. σ_c, (b) V_p vs. σ_c, and (c) $P21$ vs. σ_c.

model to assess the impact of these variables and their interaction term. We then explore the influence of $P21$ in conjunction with V_p through another regression model, adjusting for multicollinearity with PCA. Finally, we investigate the combined effect of $EQ\ L_{mean}$ and $P21$ on σ_c, employing PCA to refine the model and address collinearity concerns.

4.3.1. σ_c based on EQ L_{mean} and V_p

A multiple linear regression analysis was performed to model σ_c using $EQ\ L_{mean}$, V_p and their interaction term ($EQ\ L_{mean}$*V_p). The regression results are summarized in Fig. 7a and Table 5, and the model equation is

$$\sigma_c = -46.7608 + 0.1125\ EQL_{mean} - 0.0016V_p \left(R^2 = 0.78;\ \mathrm{F-statistics} = 16.06;\ \mathrm{RMSE} = 7.69;\ \mathrm{p-value} = 0.0001\right) \quad (2)$$

The R^2 value of 0.78 indicates that 78% of the variability in σ_c is explained by the model, which reflects a good fit. The F-statistic of 16.06 with a p-value of 0.0001 shows that the overall model is statistically significant, indicating that at least one of the predictors has a significant effect on σ_c. However, all the p-values of the predictors are bigger than the significance level (0.005). The test for multicollinearity indicated significant multicollinearity, particularly with V_p (VIF = 107.85) and the interaction term $EQ\ L_{mean}$ *V_p (VIF = 146.35), which may be causing instability in the coefficient estimates and affecting the reliability of the model.

The PCA-modified model (Table 6) indicates that while the overall model fit is robust, with an R^2 of 0.78, the individual predictors' effects on σ_c remain statistically insignificant. he p-value for $EQ\ L_{mean}$ (0.012) suggests that $EQ\ L_{mean}$ has a statistically significant individual impact on σ_c at the conventional 5% significance level. On the other hand, the p-value for V_p (0.257) indicates that V_p does not have a significant individual impact on σ_c. The F-statistic indicates that the model overall is statistically significant, showing that the predictors collectively explain a significant portion of the variability in σ_c.

4.3.2. σ_c based on P21 and V_p

A multiple linear regression analysis was conducted to model σ_c as a function of $P21$, V_p and their interaction term ($P21$*V_p). The regression model is reported in Fig. 7b and Table 7:

$$\sigma_c = 40.4780 - 9.667P21 + 0.0018V_p + 0.0004P21V_p \left(R^2 = 0.83;\ \mathrm{F-statistic} = 21.07;\ \mathrm{RMSE} = 6.9, \mathrm{p-value} = 0\right) \quad (3)$$

The model demonstrated an R-squared value of 0.83, indicating that approximately 83% of the variability in σ_c is explained by the predictors. The F-statistic of 21.07 with a p-value of 0.0000 suggests that the overall regression model is statistically significant, meaning that the predictors collectively have a meaningful relationship with σ_c. However, the effect is not highly significant for $P21$ (p-value = 0.0570) and is not statistically significant for V_p (p-value = 0.5082) and $P21$*V_p (p-value = 0.7431). One reason could be related to the sample size, or to other factors such as multicollinearity among the predictors. To assess potential multicollinearity among the predictors, VIFs were calculated (Table 7).

The VIF values indicate some level of multicollinearity, particularly for $P21$ with a VIF ≈10, which suggests that $P21$ may be correlated with the other predictors.

This collinearity could affect the stability and interpretation of the regression coefficients. In response to the multicollinearity, PCA was used to refine the model by removing the interaction term (Table 8). The results for the simplified model are as follows:

$$\sigma_c = 37.369 - 6.138P21 + 0.004709V_p \left(R^2 = 0.83;\ \mathrm{F-statistic} = 33.7;\ \mathrm{RMSE} = 6.68, \mathrm{p-value} = 0\right) \quad (4)$$

This revised model showed an R^2 of 0.83, indicating a similar level of explanatory power as the original model. The RMSE improved slightly to 6.68, reflecting a reduction in prediction error. The F-statistic of 33.7 with a p-value of 0.0000 demonstrates that the simplified model is also statistically significant. Notably, p-values for $P21$ is statistically significant (p-value = 0.002), while for V_p is not statistically significant (p-value = 0.1359). This suggests that the simplified model provides a clearer and more stable relationship between the predictors and σ_c, without the complexity introduced by the interaction term, where V_p's contribution remains insignificant.

4.3.3. σ_c based on EQ L_{mean} and P21

A multilinear regression analysis was conducted to investigate the relationship between the dependent variable σ_c and the predictors $EQ\ L_{mean}$ and $P21$, as well as their interaction term $EQ\ L_{mean}$ * $P21$. The regression model used is reported in Eq. (5) and the results of multiple linear regression are presented in Table 9 and Fig. 7c:

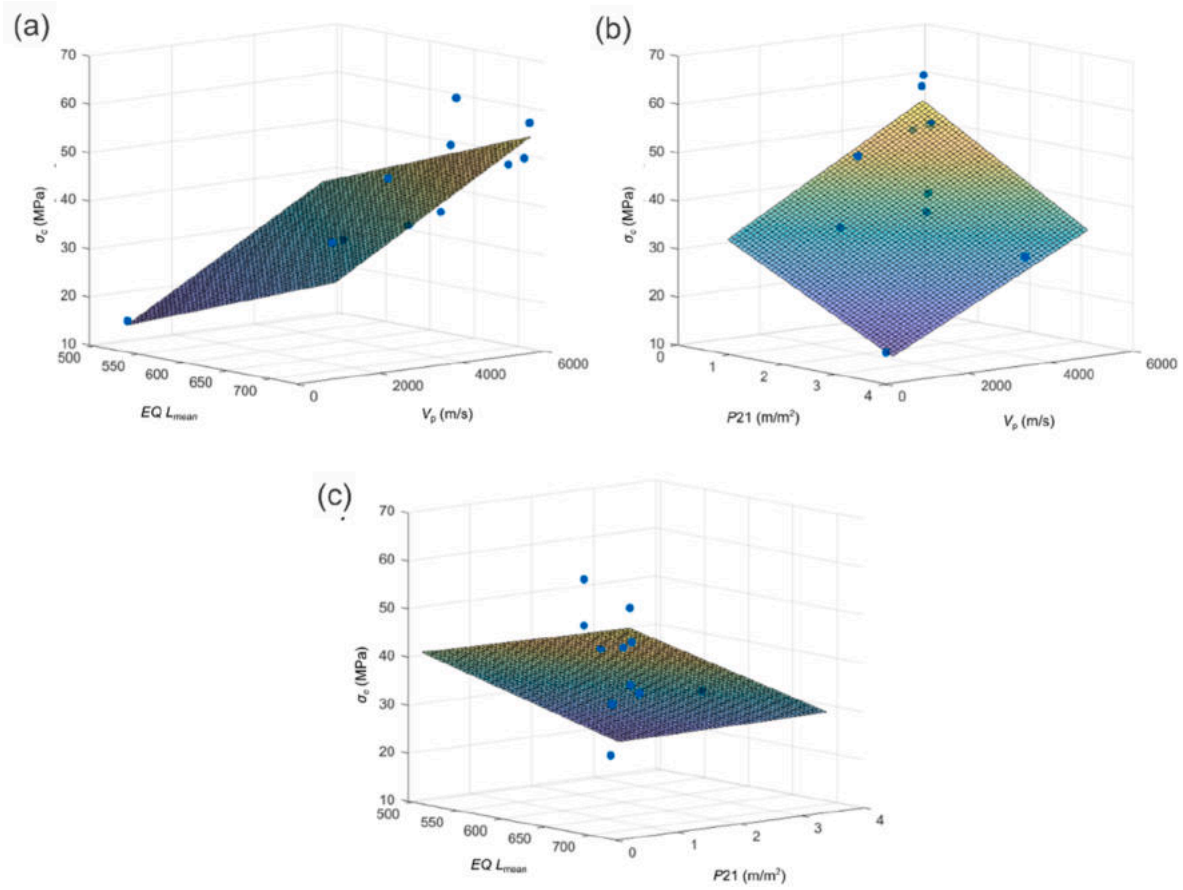

Fig. 7. Multilinear regression analyses: (a) σ_c as a function of *EQ* L_{mean} and V_p, (b) σ_c as a function of *P*21 and V_p, and (c) σ_c as a function of *EQ* L_{mean} and *P*21.

Table 5
Regression results for σ_c based on *EQ* L_{mean} and V_p.

Term	Coefficient	SE	t-statistics	p-value	VIF
Intercept	−46.7608	40.1458	−1.164	0.265	–
EQ L_{mean}	0.1125	0.0722	1.558	0.1432	7.85
V_p	−0.0016	0.0117	−0.133	0.8955	107.85
EQ L_{mean} *V_p	0	0	0.34	0.7389	146.35

Table 6
Principal Component Analysis Results for σ_c based on *EQ* L_{mean} and V_p.

Term	Coefficient	SE	t-statistics	p-value
Intercept	−57.652	23.487	−2.4546	0.027
EQ L_{mean}	0.1311	0.0456	2.8751	0.012
V_p	0.0023	0.0019	1.181	0.257

Table 7
Regression results for σ_c based on *P*21 and V_p.

Term	Coefficient	SE	t-statistics	p-value	VIF
Intercept	40.478	12.9736	3.12	0.0081	
*P*21	−9.667	4.6285	−2.0885	0.057	10.5069
V_p	0.018	0.0027	0.6803	0.5082	6.9546
*P*21*V_p	0.0004	0.0011	0.3348	0.7431	3.9935

Table 8
PCA results for σ_c based on *P*21 and V_p.

Term	Coefficient	SE	t-statistics	p-value
Intercept	37.369	8.7675	4.2622	0.0007
*P*21	−8.326	2.2466	−3.706	0.002
V_p	0.0025078	0.001585	1.5822	0.1359

Table 9
Regression results for σ_c based on *EQ* L_{mean} and *P*21.

Term	Coefficient	SE	t-statistics	p-value	VIF
Intercept	−29.211	51.3036	−0.5694	0.5788	–
EQ L_{mean}	0.1141	0.0732	1.5587	0.1431	10.0249
*P*21	8.3197	16.801	0.4952	0.6287	138.2148
EQ L_{mean} * *P*21	−0.025	0.0267	−0.9392	0.3647	95.4238

Table 10
Principal Component Analysis Results for σ_c based on *EQ* L_{mean} and *P*21.

Term	Coefficient	SE	t-statistics	p-value
Intercept	−0.51212	41.038	−0.012479	0.9902
EQ L_{mean}	0.071107	0.056882	1.2501	0.2317
*P*21	−7.1074	3.5174	−2.0206	0.0628

$$\sigma_c = -29.2110 + 0.1141 EL_{mean} + 8.319\, P21 - 0.025(EQ\, L_{mean} * P21) \left(R^2 = 0.82;\ \mathrm{F-statistics} = 21.02;\ \mathrm{RMSE} = 6.90;\ \mathrm{p-value} = 0\right) \quad (5)$$

Despite a relatively high R-squared value of 0.82, indicating that approximately 82% of the variance in the dependent variable is explained by the model, the p-values for the individual predictors were not statistically significant ($p > 0.05$), suggesting that none of the predictors or their interaction term significantly contributes to the model. The VIF values for *P*21 and the interaction term *EQ* L_{mean} * *P*21 are exceptionally high, indicating severe multicollinearity. This high collinearity likely contributes to the instability of the coefficient estimates and their lack of statistical significance. Given the multicollinearity issue, a PCA regression was performed. The estimated coefficients, standard errors, t-statistics, and p-values for this model are summarized in Table 9.

The PCA regression model (Table 10) also resulted in a high R-squared value (0.81), with a very similar RMSE compared to the original multilinear regression model (PCA regression RMSE = 6.88). However, the p-values for the predictors remained above the 0.05 threshold, indicating that even after addressing multicollinearity, the predictors were not statistically significant. This suggests that the small sample size may be limiting the statistical power to detect significant effects.

4.3.4. Bayesian Gaussian process regression results

The model was evaluated using 5-fold cross-validation with the Bayesian Gaussian Process Regression model. The cross-validation procedure yielded the following performance metrics: Mean R^2: 0.5771 ± 0.405 and Mean RMSE: 6.3304 ± 2.8797. Results indicate that, on average, the model explains 57.7% of the variance in the σ_c data, with a standard deviation of 0.405, suggesting a moderate level of consistency across the folds. The RMSE of the model's predictions was 6.33 MPa, with a standard deviation of 2.8797. This indicates that the model's predictions, on average, deviated by 6.33 MPa from the actual σ_c values, with some variability in the error across different data subsets. These results show a moderate performance of the model, with the ability to explain a significant portion of the variability in σ_c. The standard deviations in both R^2 and RMSE suggest some variability in the model's performance across different folds, which is expected in a stochastic process such as Bayesian GPR. However, the model's overall fit is reasonable given the complexity of the task and the data available.

4.4. Failure under uniaxial compression

According to Mishra and Basu (2013) and Clark and Day (2021), four failure modes were identified for brittle deformation in the samples: shear failure, axial splitting, explosive failure and combination of intact rock and discontinuities. From the results, discontinuities significantly influenced the compression failure of the sample, with the compressive strength primarily reflecting the characteristics of these mesoscopic discontinuities. In Fig. 8, the pre-failure status of the samples with discontinuity discretization (black lines) is presented together with post-failure conditions. The parameters *P*21, V_p, σ_c and *EQ* L_{mean} are reported. The mesoscopic discontinuities marked with colours before the destructive test helped us understand their role in the failure mode. In general, failure is more common along stylolites oriented at low angles to the load (stylolites shown in green and blue in Fig. 8) than along calcite-filled veins, with the concurrent formation of additional fractures in the intact rock (Fig. 8c, d, e, f, i). This may be due to the fact that stylolites are often open and filled with clay minerals (Fig. 4a and b). In some cases, failure can also occur along veins, especially if these are characterised by dissolution (Fig. 8c). In addition, the *P*21 is found to influence the failure mode as well. In a few samples characterised by high *P*21 values (Fig. 8d–i), brittle failure with disintegration into small fragments is observed. The axial splitting failure mode was instead observed for samples characterised by low *P*21 (Fig. 8h–l, m), and in which the resulting fracture planes were aligned with the direction of maximum compression, as described also by Fairhurst and Cook (1966). Shear failures occurred along persistent discontinuities oriented at an oblique angle to the loading direction (θ interval between 25° and 55° in Fig. 9b), such as in samples 3A and 3B, characterised by extensive tectonic foliation. The compressive strength values for the shear modes are the lowest across all rock samples (sample 3A with $\sigma_c = 14$ MPa and sample 3B with $\sigma_c = 30.5$ MPa). In particular, foliation aligned close to $\theta = 60°$ exhibits the most pronounced adverse effect on sample strength, rendering this angle the most critical orientation.

5. Discussion

Our results demonstrate a clear relationship between the physico-mechanical properties of the rock samples and their fracture intensity *P*21. The dynamic evolution of fracture networks under stress redistribution progressively weakens the rock. In fact, higher *P*21 values correspond to greater fracture connectivity, facilitating earlier failure at lower stress levels (Jaeger et al., 2009). Samples 1A, 1B, 1C, 2A, and 2B (rock core SC), show relatively high σ_c and EQ hardness values, alongside lower *P*21 values, indicating minimal fracturing. This suggests that the integrity of the rock significantly contributes to its strength. In contrast, samples 3A and 3B (rock core VT), exhibit the highest *P*21 values and the lowest σ_c and EQ hardness values. This evidence suggests that as fractures interact and propagate, load-bearing capacity decreases, and a transition from localised microcracks to full macroscopic rupture occurs. This correlation suggests that high fracture intensity, likely due to tectonic foliation, substantially weakens the rock. Samples 4A, 4B (rock core GT) and 5A, 5B (rock core CM) display intermediate characteristics, with moderate *P*21 values and corresponding mechanical properties.

Similarly, samples 6A–10A follow this trend, with variations in σ_c and EQ hardness aligning with the degree of fracturing observed. Samples 6A and 8A exhibit the lowest σ_c values (8.5 MPa and 15.9 MPa, respectively), alongside high *P*21 values (3.4 m/m^2 and 3 m/m^2). This suggests that extensive fracturing significantly reduces rock strength. Conversely, sample 10A shows the highest σ_c value (62.2 MPa) and the lowest *P*21 (0.1 m/m^2), reinforcing the notion that a lower fracture density is associated with higher mechanical strength. The other samples (7A, 9A, and 9B) present intermediate values, with σ_c ranging between 26.4 MPa and 46.7 MPa, indicating a moderate correlation between fracture intensity and strength. Overall, the data underscore the significant impact of fracture intensity on rock strength, with higher fracturing leading to decreased σ_c and increased variability in hardness measurements. With regards to failure modes high *P*21samples

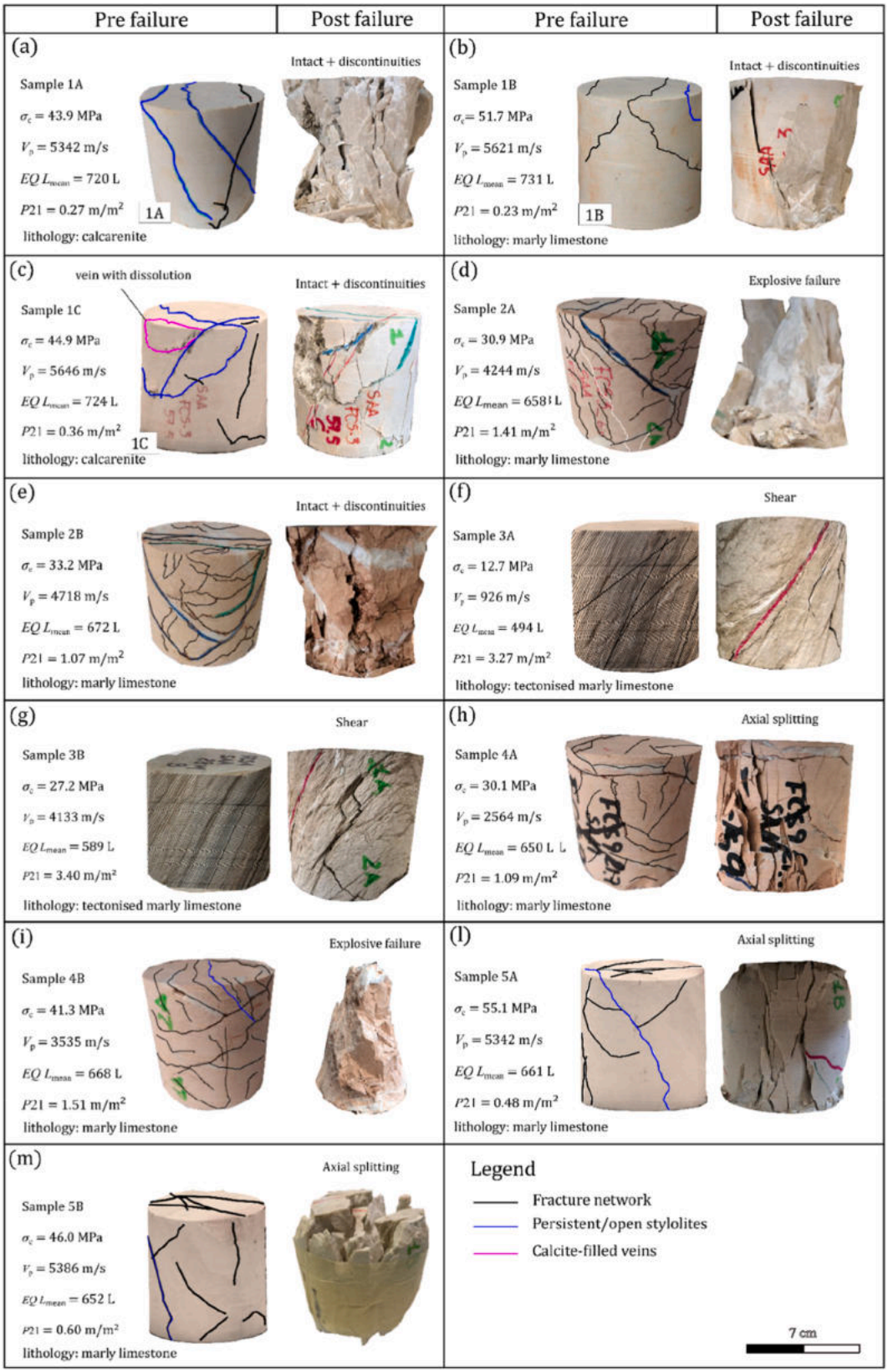

Fig. 8. Overview of the pre- and post-failure condition with results of destructive and non-destructive tests, and the *P*21 for some samples: (a) Sample 1A, (b) Sample 1B, (c) sample 1C, (d) Sample 2A, (e) Sample 2B, (f) Sample 3a, (g) Sample 3B, (h) Sample 4A, (i) Sample 4B, (l) Sample 5A, and (m) Sample 5B.

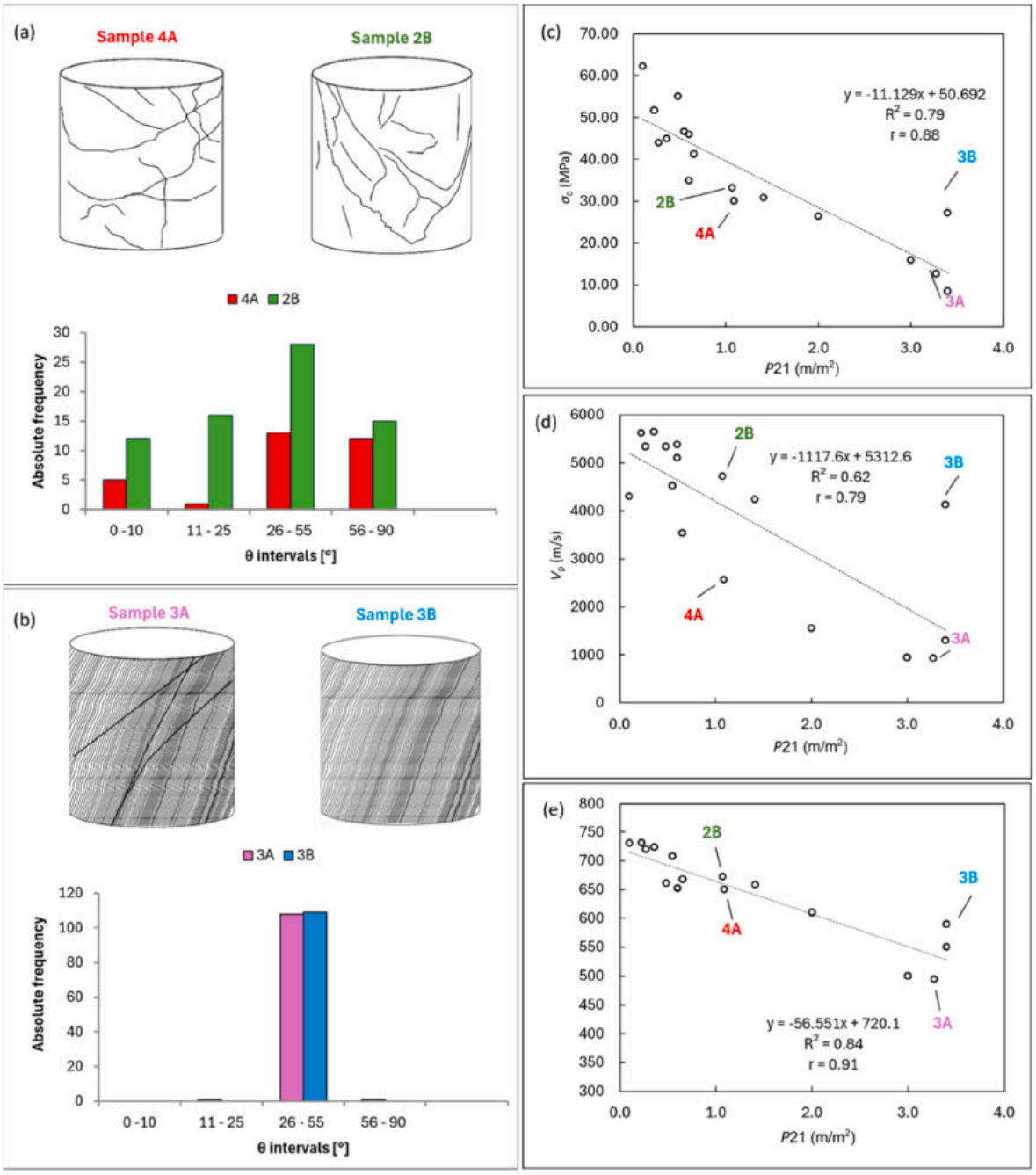

Fig. 9. (a) histogram of discontinuities inclination (ϑ intervals) for samples 2A and 4B with a schematic representation of the fracture network, (b) histogram of discontinuities inclination (ϑ intervals) for samples 3A and 3B with a schematic representation of the fracture network, (c) $P21/\sigma_c$ relationship, (d) $P21/V_p$ relationship, and (e) $P21/EQ\ L_{mean}$ relationship.

fail explosively due to rapid fracture coalescence, while low $P21$ samples predominantly show axial splitting, indicating gradual crack propagation. This highlights that strength degradation is controlled by both fracture density and dynamic crack interaction.

According to the correlation results, non-destructive techniques like EQ and ultrasonic P-wave velocity tests are deemed valuable for predicting the strength of fractured rock samples under uniaxial compression. In the literature, both linear and nonlinear simple regression analyses have been proposed for exploring empirical relationships among mechanical properties of rocks. For instance, several authors (Tuğrul and Zarif, 1999; Yasar and Erdogan, 2004; Sharma and Singh, 2008; Mishra and Basu, 2013) suggested linear correlations between V_p and σ_c in sandstones, while others (Karakus and Tutmez, 2006; Yilmaz and Yuksek, 2009; Monjezi et al., 2012) proposed multiple regression equations from index test results to predict σ_c of rock materials. Despite both simple and multilinear regression models demonstrated comparable robustness based on statistical parameters, the multilinear model resulted in a more comprehensive and accurate model to explain variation in the outcome variable (Figs. 6 and 7), as also reported by (Mishra and Basu, 2013). However, our study reveals that multicollinearity among predictors, particularly with

V_p, affects model stability, necessitating the use of PCA and Bayesian GPR for improved prediction accuracy. The comparison of multiple regression models revealed significant insights into the relationship between σ_c and the predictors *EQ* L_{mean}, V_p, and *P*21. The original models demonstrated high R^2 values, indicating a good overall fit but the p-values for individual predictors were consistently high, suggesting that the predictors were not statistically significant. High VIF values in models involving V_p and the interaction terms indicated severe multicollinearity, contributing to the instability of the coefficient estimates. In response, PCA was employed to address collinearity issues, resulting in slightly lower RMSE values but still insignificant p-values for the predictors. In contrast, the Bayesian GPR model yielded a mean R^2 of 0.5771 ± 0.405 and an RMSE of 6.3304 ± 2.8797, demonstrating moderate predictive power and a balance between flexibility and robustness. These results highlight that the small sample size may likely limiting the statistical power of the models, making it difficult to detect significant effects of the predictors on σ_c. The PCA-modified models provided clearer relationships by reducing multicollinearity in modelling σ_c based on *P*21 and V_p, yet the need for a larger sample size remains crucial for more reliable and statistically significant results. The integration of Bayesian GPR allowed for a comparative evaluation of the models, revealing that while multilinear regression and PCA-based models offer interpretable relationships between variables, Bayesian GPR provides a more adaptive approach by incorporating non-linearity and uncertainty into predictions. Furthermore, the inclusion of new samples (6A–10A) confirms the robustness of previous findings, particularly regarding the role of fracture intensity in reducing σ_c. The results suggest that while multilinear regression and PCA help address multicollinearity, the inclusion of Bayesian GPR enhances model robustness, mitigating overfitting issues associated with small sample sizes. The findings reinforce the necessity of combining multiple analytical approaches to obtain a more comprehensive understanding of rock strength variations. Future studies should consider expanding the dataset to further validate these trends and improve model generalization.

Considering that the porosity of the Scaglia Rossa Fm. samples is negligible, our results indicate that discontinuities have a significant impact on the compression failure of the sample. The compressive strength predominantly reflects the fracture intensity degree and the properties of the mesoscopic discontinuities, this being consistent with the findings by Pappalardo (2015). In addition, the orientation of fractures (θ) appears to play a role in failure mechanisms. Although a quantitative correlation could not be established due to data limitations, qualitative observations suggest that samples with lower fracture inclinations (<30°–40°) predominantly fail by shear along discontinuity planes, while those with higher inclinations exhibit axial splitting or a mixed failure mode. These trends align with previous studies on anisotropic failure behaviour in fractured rocks (Jaeger et al., 2009; Zhu et al., 2021). This further highlights the importance of considering fracture geometry in rock strength assessments.

The strong negative correlation between *P*21 and σ_c (Fig. 6c–Table 4) is consistent with numerous previous studies relating the increase of fracture intensity to a strong reduction of rock matrix integrity (e.g., Barton et al., 1974; Hudson and Dusseault, 1989; Jaeger et al., 2009). In the analysed samples, fracture intensity is controlled by the occurrence of stylolites, cleavage, joints, and veins, which are related to the tectonic deformation of the area, and other factors such as bedding thickness, lithology, and texture characteristics (Pireh et al., 2015). It is commonly observed that pressure solution features, such as stylolites, highly frequent in carbonates (Tada and Siever, 1989), align with the susceptibility of minerals to pressure solution (Heald, 1955), increasing the total amount of clay-rich minerals in the rock. In line with previous findings, results of calcimetry analyses (Table 11) have shown progressive accumulation of non-soluble (often clay-rich) residue on the stylolitic planes and joints with a progressive increase of *P*21, resulting in a relative decrease in $CaCO_3$. Failure predominantly occurred along stylolites oriented at low angles to the load, rather than along calcite-filled veins, especially if stylolites are open and filled with clay minerals. Moreover, failure along veins occurred predominantly in those characterized by dissolution processes (Fig. 8c). Foliation aligned near $\theta = 60°$ demonstrates a significant impact on sample strength, suggesting this angle may be critical. This observation is in line with the evidence of (Jaeger et al., 2009), observing that failure under uniaxial compression occurs along foliation when it is oriented within θ angles ranging from 35° to 81°.

Table 11
Results of calcimetric analysis with indication of *P*21 for each rock sample analysed.

Rock core	Rock sample	$CaCO_3$ (%)	Non-soluble minerals (%)	*P*21 (m/m^2)
SC	1C	95	5	0.36
SC	2A	99	1	1.41
VT	3A	82	18	3.27
GT	4B	81	19	3.4
CM	5A	91	9	0.48
CM	6A	99.3	1	3.4
RC	7A	70.1	30	2
CM	8A	98.1	2	3
SC	9B	82	18	0.55
RC	10A	76.3	24	0.1

5.1. Controls of tectonic deformation on rock strength

This study investigated distinct lithotypes belonging to calcareous rocks, i.e., calcarenites, crystalline limestones and marly limestones, in a fold and thrust belt setting. As reported by Tavani et al. (2012), fracture network evolution is influenced not only by lithology but also by deformation history. Fractures formed in early tectonic stages may later be reactivated, extended, or rotated, altering fracture connectivity and stress distribution. In particular, the examined samples were taken in the anticline hinge area, overturned limb area, the thrust zone and syncline hinge area. These distinct structural zones display their specific structural assemblages (Tavani et al., 2015). Despite the different structural positions, similar deformation features (i.e., bed-parallel stylolites, tectonic stylolites, calcite veins) occur in all the studied samples, although with variable occurrence in terms of cumulative number (Fig. 8, *P*21). As our study focuses on limestone beds, the structural control on the density of pressure-solution seams and stytlolites must be taken into account. Bedding-parallel stylolites, being burial-related, are essentially independent on structural position within folds. They may have been enhanced by post-diagenetic pressure-solution in fold limbs that rotated by fold amplification to acquire a new position prone to bedding-normal shortening, such a case was possible to observe in Sample 2A. Similar spaced, disjunctive pressure-solution cleavage (i.e. tectonic stylolites) develops mostly by initial layer-parallel shortening predating fold amplification and is only slightly modified during fold amplification (Tavani et al., 2012). This resulted in a widespread occurrence of spaced tectonic stylolites in limestones, almost irrespective of the position – limb or hinge regions – within regional, map-scale folds. However, their reactivation during later deformation increases fracture connectivity, reducing rock strength. Pressure solution along stylolites removes load-bearing material and increases clay mineral content, lowering cohesion and promoting further fracturing. Of course, local development of more intense

cleavage is observed in the inner-arc zones of hinge regions of minor, parasitic (meter-scale) close to tight folds. Such parasitic folds while extensional fractures/veins occur in the outer-arc zones (as a result of tangential-longitudinal strain; Ramsay, 1967); however, such region was avoided by our sampling. We observed varying mechanical responses of these lithotypes to tectonic deformation, leading to differences in the presence, frequency, and types of discontinuities. Notable variations include calcarenites exhibiting fewer structural features, with stylolites typically displaying smaller amplitudes and indentations, and containing less argillaceous material at the interface (Fig. 4a–c). The paucity of insoluble material can be attributed to the original lithology prior to deformation. Another significant factor influencing not only the strength of rocks but also the velocity of ultrasonic P-waves is the orientation of discontinuity surfaces relative to the UCS load and P-wave propagation direction. Extensive research has been undertaken to investigate the factors contributing to this phenomenon, including examination of mechanical anisotropy (Schoenberg and Sayers, 1995; Barton, 2006), suggesting that the orientation and density of discontinuities and pores may play a role on the wave velocity anisotropy (In'kov et al., 2005; Azhari, 2013; Petružálek et al., 2013; Lokajíček and Svitek, 2015; Ding et al., 2019; Zhukov and Kuzmin, 2020; Zhao et al., 2023), as well as the infilling material of joints or bedding planes (Barton, 2006). In this regard, this study has elucidated that, at the same values of parameter $P21$ (Fig. 9), markedly different V_p outcomes can occur, even within the same segment of rock core.

Frequency histograms are presented with a schematic representation of the fracture network, in which the inclination of discontinuities with respect to the vertical (direction of UCS load and P-wave propagation direction, $\theta = 0^\circ$) is reported. Sample 2B notably presents a higher percentage of discontinuities with orientations between 11° and 25°, known to enhance P-wave propagation (Azhari, 2013). Conversely, the reduction in V_p observed in sample 4A can be attributed to the presence of thick calcite veins oriented perpendicular to the direction of P-wave propagation (Fig. 9). In fact, based on the findings of Azhari (2013) and Abbass et al. (2018), fractures parallel to the propagation direction ($\theta = 0^\circ$) marginally enhance V_p, serving as significant waveguides, whereas fractures at 45° cause less reduction in V_p compared to those at 25° and 90°. A similar behaviour can be observed in rock samples 3A and 3B, originating from the same rock core segment, in which, at the same value of parameter $P21$, distinct variations in V_p responses are evident (Fig. 9d). Despite both samples exhibiting pronounced tectonic cleavage inclined at 50° (depicted by the blue class in Fig. 9b), sample 3A is traversed by two sets of calcite-filled veins (Fig. 9b), resulting in a discernible reduction in V_p values. Notably, these features hold negligible significance for σ_c (Fig. 9e) and yield no substantial deviation in EQ values. These observations underscore the necessity for caution when employing ultrasound P-wave velocity measurements in the analysis of rock samples with different density and orientation of discontinuities. As elucidated by prior studies (Clark and Day, 2021), these veins may not represent preferential planes for failure, despite they are critically oriented within the zone of foliation failure (Jaeger et al., 2009) as the cementation within the vein structure can potentially augment rather than diminish the strength.

6. Conclusions

This study explores the influence of tectonic deformation on rock strength using a combination of destructive (UCS test) and non-destructive (EQ, ultrasound P-wave velocity) methods. By analysing 11 rock samples from the northern Apennines, locate in different structural positions with respect to fold, fault, and thrust structures, we demonstrated the effectiveness of non-destructive testing, particularly the EQ, in evaluating rock strength of fractured samples in the laboratory. Our results reveal a strong linear correlation between EQ values and σ_c, as well as between V_p and σ_c. Notably, the highest correlation for σ_c prediction was achieved through a multiple regression model integrating both non-destructive techniques, highlighting the complementary role of EQ and ultrasound measurements in geotechnical assessments. We also identified the critical role of fracture intensity ($P21$), as measured through photogrammetric analysis, in influencing rock strength. As fracture intensity increases, particularly through stylolites and pressure-solution cleavage, the rock's mechanical properties are notably affected, leading to a decrease in strength and an increase in clay mineral content. This has significant implications for the reliability of engineering structures in areas with similar deformation histories. The analysis of fracture orientations further confirms that V_p values are highly sensitive to the alignment of fractures, particularly in samples where fractures are at high angles to the P-wave direction, further emphasizing the importance of considering fracture networks when evaluating rock mass properties. Although the relatively small size of the sample involves limitations, particularly in the regression analysis, the findings of this study underline the utility of integrating non-destructive techniques like the EQ in engineering geology. The results suggest that EQ hardness, alongside P-wave velocity, can provide valuable, cost-effective insights into rock mass strength and failure behaviour, essential for infrastructure development in complex geological settings. Future studies with larger sample sets would help to refine these models, enhancing the predictive power and applicability of these techniques in engineering projects.

CRediT authorship contribution statement

Elisa Mammoliti: Writing – original draft, Methodology, Conceptualization, Writing – review & editing, Project administration, Data curation, Validation, Investigation. **Danica Jablonská:** Writing – original draft, Investigation, Methodology, Validation, Conceptualization. **Antonio Ferretti:** Writing – original draft, Writing – review & editing, Investigation, Methodology. **Michele Morici:** Methodology, Writing – review & editing, Investigation. **Stefano Mazzoli:** Supervision, Validation, Writing – review & editing, Resources. **Mirko Francioni:** Validation, Investigation, Writing – review & editing, Methodology, Supervision.

Funding

The study has been financially supported by the company Cicli Integrati Impianti Primari "CIIP", Italy. The support was granted to the Co-author Stefano Mazzoli (Grant No. STC10006-CIIP SPA 2020), Reti idropotabili Materazzi M. - vincolo numero 262/2020/ST. If there are other authors, they declare that they have no known competing financial interests or personal relationships that could have appeared to influence the work reported in this paper.

Data availability

All data is provided as figures and tables in the manuscript.

Declaration of competing interest

The authors declare that they have no known competing financial interests or personal relationships that could have appeared to influence the work reported in this paper.

Acknowledgements

The authors are grateful to Italferr S.p.A. for providing rock cores for the analyses and to Dr. Veronica Gironelli to support the first phase of data collection. The authors also thank S.T.S. Mobile S.r.l. for preparing the samples of the uniaxial compression tests, and Prof. Jacopo Donnini of Università Politecnica delle Marche for performing the UCS tests. Many thanks also to Prof. Alessandra Negri and Dr. Francesca Caridi from Università Politecnica delle Marche for conducting the calcimetric analysis.

References

Abbass, H.A., Mohamed, Z., Yasir, S.F., 2018. A review of methods, techniques and approaches on investigation of rock anisotropy. AIP Conf. Proc. 2020 (1), 020012.

Agisoft, 2020. In: Agisoft Metashape User Manual, Professional edition. version 1.6. https://www.agisoft.com/pdf/metashape-pro_1_6_en.pdf. (Accessed 10 June 2023).

Aldeeky, H., Al Hattamleh, O., Rababah, S., 2020. Assessing the uniaxial compressive strength and tangent Young's modulus of basalt rock using the leeb rebound hardness test. Mater. Construcción 70 (340), 230.

Aliabdo, A.A.E., 2012. Reliability of using nondestructive tests to estimate compressive strength of building stones and bricks. Alex. Eng. J. 51, 193–203.

Aoki, H., Matsukura, Y., 2008. Estimating the unconfined compressive strength of intact rocks from equotip hardness. Bull. Eng. Geol. Environ. 67 (1), 23–29.

Askaripour, M., Saeidi, A., Mercier-Langevin, P., Rouleau, A., 2022. A review of relationship between texture characteristic and mechanical properties of rock. Geotechnics 2 (1), 262–296.

ASTM D2845-05, 2005. Standard Test Method for Laboratory Determination of Pulse Velocities and Ultrasonic Elastic Constant of Rock. ASTM International, West Conshohocken, PA, USA.

ASTM D2938-79, 1980. Standard Method of Test for Unconfined Compressive Strength of Rock Core Specimens. ASTM International, West Conshohocken, PA, USA.

Azhari, H.E., 2013. Effect of the Number and Orientation of Fractures on the P-wave Velocity Diminution: Application on the Building Stones of the Rabat Area (Morocco), vol. 3, pp. 71–81. GM.

Azimian, A., 2017. Application of statistical methods for predicting uniaxial compressive strength of limestone rocks using nondestructive tests. Acta Geotech 12, 321–333.

Aydin, A., Basu, A., 2005. The schmidt hammer in rock material characterization. Eng. Geol. 81 (1), 1–14.

Barton, N., 1973. Review of a new shear-strength criterion for rock joints. Eng. Geol. 7, 287–332.

Barton, N., 2006. Rock Quality, Seismic Velocity, Attenuation and Anisotropy. Balkema-proceedings and Monographs in Engineering, Water and Earth Sciences. Taylor & Francis, London; New York.

Barton, N., Lien, R., Lunde, J., 1974. Engineering classification of rock masses for the design of tunnel support. Rock Mech. 6, 189–236.

Baud, P., Rolland, A., Heap, M.J., Xu, T., Nicolé, M., Ferrand, T., Reuschlé, T., Toussaint, R., Conil, N., 2016. Impact of stylolites on the mechanical strength of limestone. Tectonophysics 690, 4–20.

Baud, P., Wong, T., Zhu, W., 2014. Effects of porosity and crack density on the compressive strength of rocks. Int. J. Rock Mech. Min. Sci. 67, 202–211.

Bernoulli, D., Jenkyns, H.C., 1974. Alpine, Mediterranean, and Central Atlantic Mesozoic Facies in Relation to the Early Evolution of the Tethys, vol. 19. SEPM Spec. Publ.

Bewick, R.P., Amann, F., Kaiser, P.K., Martin, C.D., 2015. Interpretation of UCS test results for engineering design. In: Proc. ISRM Congress 2015 – Int'L Symposium on Rock Mechanics. Sydney, Australia. ISBN: 978-1-926872-25-4.

Bice, D.M., Montanari, A., Rusciadelli, G., 2007. Earthquake-induced turbidites triggered by sea level oscillations in the Upper Cretaceous and Paleocene of Italy. Terra Nova 19, 387–392.

Bieniawski, Z.T., 1973. Engineering classification of jointed rock masses. Civ. Eng. Siv. Inge. 1973 (12), 335–343.

Bieniawski, Z.T., Bernede, M.J., 1979. Suggested methods for determining the uniaxial compressive strength and deformability of rock materials: part 1. Suggested method for determining deformability of rock materials in uniaxial compression. Int. J. Rock Mech. Min. Sci. Geomech. Abstr. 16 (2), 135–140.

Brady, B.H., Brown, E.T., 2006. Rock Mechanics for Underground Mining, third ed. Springer, Dordrecht, Netherlands.

Brideau, M.A., Yan, M., Stead, D., 2009. The role of tectonic damage and brittle rock fracture in the development of large rock slope failures. Geomorphology 103, 30–49.

Brozovsky, J., 2014. Determine the compressive strength of calcium silicate bricks by combined nondestructive method. Sci. World J. 2014, 1–5.

Calamita, F., Cello, G., Deiana, G., Paltrinieri, W., 1994. Structural styles, chronology rates of deformation, and time-space relationships in the umbria-marche thrust system (central apennines, Italy). Tectonics 13, 873–881.

Cao, R., Cao, P., Lin, H., Fan, X., Zhang, C., Liu, T., 2019. Crack Initiation, Propagation, and Failure Characteristics of Jointed Rock or Rock-Like Specimens: A Review. *Adv. Civ. Eng.* 2019.

Cello, G., Mazzoli, S., Tondi, E., Turco, E., 1997. Active tectonics in the central apennines and possible implications for seismic hazard analysis in peninsular Italy. Tectonophysics 272 (1), 43–68.

Centamore, E., Chiocchini, M., Deiana, G., Micarelli, A., Pieruccini, U., 1971. Contributo alla conoscenza del Giurassico dell'Appennino umbro-marchigiano. Stud. Geol. Camerti (1), 7–90. + 2 carte.

Cilona, A., Faulkner, D.R., Tondi, E., Agosta, F., Mancini, L., Rustichelli, A., Baud, P., Vinciguerra, S., 2014. The effects of rock heterogeneity on compaction localization in porous carbonates. J. Struct. Geol. 67, 75–93.

Clark, M.D., Day, J.J., 2021. Mineralogical and sample selection implications for geomechanical properties of intact heterogeneous and veined rocks from the legacy skarn deposit. Eng. Geol. 285, 106067.

Colacicchi, R., Passeri, L., Pialli, G., 1970. Nuovi dati sul giurese umbro-marchigiano ed ipotesi per un suo inquadramento regionale. Mem. Soc. Geol. It. 9, 839–874.

Coombes, M.A., Feal-Pérez, A., Naylor, L.A., Wilhelm, K., 2013. A non-destructive tool for detecting changes in the hardness of engineering materials: application of the equotip durometer in the coastal zone. Eng. Geol. 167, 14–19.

Correns, C.W., 1968. Über die Herkunft der Elemente in Sedimentgesteinen. Geol. Rundsch. 58, 365–378.

Deiana, G., Pialli, G., 1994. The structural provinces of the umbro-marchean apennines. Mem. Soc. Geol. Ital. 48, 473–484.

Dershowitz, W.S., Herda, H.H., 1992. Interpretation of fracture spacing and intensity. In: Proc. 33rd U.S. Symp. Rock Mech. (USRMS). Santa Fe, NM, Paper ARMA-92-0757.

Desarnaud, J., Kiriyama, K., Bicer Simsir, B., Viles, H.A., et al., 2019. A laboratory study of Equotip surface hardness measurements on a range of sandstones: What influences the values and what do they mean? Earth Surf. Process. Landforms. 44 (7), 1419–1429.

Ding, P., Wang, D., Di, G., Li, X., 2019. Investigation of the effects of fracture orientation and saturation on the Vp/Vs ratio and their implications. Rock Mech. Rock Eng. 52 (9), 3293–3304.

Dunham, R.J., 1962. Classification of carbonate rocks according to depositional texture. In: Ham, W.E. (Ed.), Classification of Carbonate Rocks. AAPG Memoir 1. AAPG, Tulsa, pp. 108–121.

Einstein, H.H., Dershowitz, W.S., 1990. Tensile and shear fracturing in predominantly compressive stress fields. Eng. Geol. 29, 149–172.

Fairhurst, C., Cook, N.G.W., 1966. The of maximum phenomenon of rock splitting parallel to the direction compression in the neighbourhood of a surface, *in: ISRM Congress*. ISRM, p. ISRM-1CONGRESS-1966-115.

Girardeau-Montaut, D., 2016. Cloudcompare. EDF R&D. Telecom ParisTech, France. Version 11(5).

Gomez-Heras, M., Benavente, D., Pla, C., Martinez-Martinez, J., Fort, R., Brotons, V., 2020. Ultrasonic pulse velocity as a way of improving uniaxial compressive strength estimations from leeb hardness measurements. Constr. Build. Mater. 261, 119996.

Greco, R., Sorriso-Valvo, M., 2005. Relationships between joint apparent separation, schmidt hammer rebound value, and distance to faults, in rocky outcrops, Calabria, southern Italy. Eng. Geol. 78 (3–4), 309–320.

Hawkins, A.B., 1998. Aspects of rock strength. Bull. Eng. Geol. Environ. 57 (1), 17–30.

Hawkins, A. B., and McConnell, B. J. 1992. Sensitivity of sandstone strength and deformability to changes in moisture content. Q. J. Eng. Geol. 25(2), 115–130.

Heald, M.T., 1955. Stylolites in sandstones. J. Geol. 63 (2), 101–114.

Hoek, E., Martin, C.D., 2014. Application and limits of the Hoek–Brown criterion for fractured rock masses. J. Rock Mech. Geotech. Eng. 11 (3), 445–463.

Hudson, J.A., Dusseault, M.B., 1989. Rock Engineering. Mc Graw-Hill International Editions, New York, p. 14.

In'kov, V.N., Cherepetskaya, E.B., Shkuratnik, V.L., Karabutov, A.A., Makarov, V.A., 2005. Ultrasonic laser spectroscopy of mechanic-acoustic nonlinearity of cracked rocks. J. Appl. Mech. Tech. Phys. 46, 452–457.

Jaeger, J.C., Cook, N.G., Zimmerman, R., 2009. Fundamentals of Rock Mechanics, fourth ed. John Wiley & Sons, Chichester.

Kahraman, S., 2001. A correlation between P-wave velocity, number of joints and schmidt hammer rebound number. Int. J. Rock Mech. Min. Sci. 38 (5), 729–733.

Karakus, M., Tutmez, B., 2006. Fuzzy and multiple regression modelling for evaluation of intact rock strength based on point load, schmidt hammer and sonic velocity. Rock Mech. Rock Eng. 39, 45–57.

Kawasaki, S., Tanimoto, C., Koizumi, K., Ishikawa, M., 2002. An attempt to estimate mechanical properties of rocks using the equotip hardness tester. J. Jpn. Soc. Eng. Geol. 43 (4), 244–248.

Kompatscher, M., 2004. Equotip-rebound hardness testing after D. Leeb. In: Proc. HARDMEKO 2004 – Hardness Measurements Theory and Application in Laboratories and Industries, pp. 11–12. November, Washington, D.C., USA.

Kovler, K., Wang, F., Muravin, B., 2018. Testing of concrete by rebound method: leeb versus schmidt hammers. Mater. Struct. 51, 138.

Lee, H., Jeon, S., 2011. An experimental and numerical study of fracture coalescence in pre-cracked specimens under uniaxial compression. Int. J. Solids Struct. 48 (6), 979–999.

Li, Y., et al., 2021. Size-effect in brittle fracture of shale specimens. Nat. Resour. Res. 30 (6), 4439–4456.

Lokajíček, T., Svitek, T., 2015. Laboratory measurement of elastic anisotropy on spherical rock samples by longitudinal and transverse sounding under confining pressure. Ultrasonics 56, 294–302.

Mammoliti, E., Cupido, M., Teloni, R., Tittarelli, F., Giuli, G., Paris, E., Farabollini, P., Santini, S., 2024. Implementation of a non-destructive method to assess weathering deterioration of sandstones in cultural heritage. Bull. Eng. Geol. Environ. 83, 110.
Mammoliti, E., Ferretti, A., Malavolta, M., Teloni, R., Ruggeri, P., Roselli, G., 2021. Defining a non-destructive in situ approach for the determination of historical mortar strength using the equotip hardness tester. Appl. Sci. 11 (11), 4788.
Marchegiani, L., Bertotti, G., Cello, G., Deiana, G., Mazzoli, S., Tondi, E., 1999. Pre-orogenic tectonics in the Umbria–Marche sector of the afro-adriatic Continental margin. Tectonophysics 315, 123–143.
Mishra, D.A., Basu, A., 2013. Estimation of uniaxial compressive strength of rock materials by index tests using regression analysis and fuzzy inference system. Eng. Geol. 160, 54–68.
Mogi, K., 2006. Experimental Rock Mechanics, 1st Edition. CRC Press, London, p. 375–pages.
Monjezi, M., Amini Khoshalan, H., Razifard, M., 2012. A neuro-genetic network for predicting uniaxial compressive strength of rocks. Geotech. Geol. Eng. 30, 1053–1062.
Morgan, S., Law, R., de Saint Blanquat, M., 2013. Forceful emplacement of the Eureka Valley-Joshua Flat–Beer Creek composite pluton into a structural basin in eastern California; internal structure and wall rock deformation. Tectonophysics 608, 753–773.
Pappalardo, G., 2015. Correlation between P-wave velocity and physical–mechanical properties of intensely jointed dolostones, peloritani mounts, NE sicily. Rock Mech. Rock Eng. 48 (4), 1711–1721.
Park, K., Bobet, A., 2010. Crack coalescence in specimens with multiple cracks. Eng. Fract. Mech. 77 (15), 2726–2738.
Petružálek, M., Vilhelm, J., Rudajev, V., Lokajíček, T., Svitek, T., 2013. Determination of the anisotropy of elastic waves monitored by a sparse sensor network. Int. J. Rock Mech. Min. Sci. 60, 208–216.
Pireh, A., Alavi, S.A., Ghassemi, M.R., Shaban, A., 2015. Analysis of natural fractures and effect of deformation intensity on fracture density in garau formation for shale gas development within two anticlines of zagros fold and thrust belt, Iran. J. Pet. Sci. Eng. 125, 162–180.
Poblet, J., Bulnes, M., Uzkeda, H., Magán, M., 2022. Using the schmidt hammer on folds: an example from the cantabrian zone (NW iberian peninsula). J. Struct. Geol. 155, 104512.
Priest, S.D., Hudson, J.A., 1976. Discontinuity spacings in rock. Int. J. Rock Mech. Min. Sci. Geomech. Abstr. 13 (5), 135–148.
Proceq, S.A., 1977. Equotip Operations Instructions. Zurich: PROCEQ SA Zurich, Switzerland.
Ramsay, J.G., 1967. Folding and Fracturing of Rocks. McGraw-Hill, New York, p. 568.
Sarfarazi, V., Haeri, H., 2016. Estimation of brittleness indexes from petrographic characteristics of different sandstone types. Comput. Concr. 17 (1), 107–127.
Sbartaï, Z.M., Breysse, D., Larget, M., Balayssac, J.P., 2012. Combining NDT techniques for improved evaluation of concrete properties. Cem. Concr. Compos. 34 (6), 725–733.
Schoenberg, M., Sayers, C.M., 1995. Seismic anisotropy of fractured rock. Geophysics 60 (1), 204–211.
Sharma, P.K., Singh, T.N., 2008. A correlation between P-wave velocity, impact strength index, slake durability index and uniaxial compressive strength. Bull. Eng. Geol. Environ. 67 (1), 17–22.
Tada, R., Siever, R., 1989. Pressure solution during diagenesis. Annu. Rev. Earth Planet Sci. 17, 89–118.
Tavani, S., Storti, F., Bausà, J., Muñoz, J.A., 2012. Late thrusting extensional collapse at the Mountain front of the northern apennines (italy). Tectonics 31, TC3009.
Tavani, S., Storti, F., Lacombe, O., Corradetti, A., Muñoz, J.A., Mazzoli, S., 2015. A review of deformation pattern templates in foreland basin systems and fold-and-thrust belts: implications for the state of stress in the frontal regions of thrust wedges. Earth Sci. Rev. 141, 82–104.
Theodoridou, M., Dagrain, F., Ioannou, I., 2015. Micro-destructive cutting techniques for the characterization of natural limestone. Int. J. Rock Mech. Min. Sci. 76, 98–103.
Török, Á., Vásárhelyi, B., 2010. Estimation of the strength of rocks using the Schmidt hammer rebound method. Eng. Geol. 85 (1–2), 1–8.
Toussaint, R., Aharonov, E., Koehn, D., Gratier, J.-P., Ebner, M., Baud, P., Renard, F., 2018. Stylolites: a review. Journal of Structural Geology 114, 163–195.
Tsoutrelis, C.E., Exadaktylos, G.E., 1993. Effect of rock discontinuities on certain rock strength and fracture energy parameters under uniaxial compression. Geotech. Geol. Eng. 11, 81–105.
Tuğrul, A., Zarif, I.H., 1999. Correlation of mineralogical and textural characteristics with engineering properties of selected granitic rocks from Turkey. Eng. Geol. 51 (4), 303–317.
Tuncay, E., Hasancebi, N., 2009. The effect of length to diameter ratio of test specimens on the uniaxial compressive strength of rock. Bull. Eng. Geol. Environ. 68, 491–497.
Verwaal, W., Mulder, A., 1993. Estimating rock strength with the equotip hardness tester. Int. J. Rock Mech. Min. Sci. Geomech. Abstr. 30 (6), 659–662.
Wang, Z., Li, W., Wang, Q., Liu, S., Hu, Y., Fan, K., 2019. Relationships between the petrographic, physical and mechanical characteristics of sedimentary rocks in Jurassic weakly cemented strata. Environ. Earth Sci. 78, 131.
Wong, T.-F., 2013. Micromechanics of faulting and failure in porous rocks. Annu. Rev. Earth Planet. Sci. 41, 533–567.
Wong, L.N.Y., Einstein, H.H., 2009. Process zone development associated with cracking processes in Carrara marble. Proc. 9th Int. Conf. Anal. Discont. Deform.: New Dev. Appl. 581–588.
Wyllie, M.R.J., Gregory, A.R., Gardner, G.H.F., 1956. Elastic wave velocities in heterogeneous and porous media. Geophysics 21 (1), 41–70.
Yasar, E., Erdogan, Y., 2004. Correlating sound velocity with the density, compressive strength and Young's modulus of carbonate rocks. Int. J. Rock Mech. Min. Sci. 41 (5), 871–875.
Yilmaz, N.G., Goktan, R.M., 2019. Comparison and combination of two NDT methods with implications for compressive strength evaluation of selected masonry and building stones. Bull. Eng. Geol. Environ. 78, 4493–4503.
Yilmaz, I., Yuksek, G., 2009. Prediction of the strength and elasticity modulus of gypsum using multiple regression, ANN, and ANFIS models. Int. J. Rock Mech. Min. Sci. 46 (4), 803–810.
Zhang, H., et al., 2020. Machine-learning prediction of UCS from hardness and point-load index testing. Rock Mech. Rock Eng. 53 (7), 3293–3309.
Zhao, Y., Li, Q., Zhang, K., Yang, Y., Gu, X., 2023. Effect of fissure angle on energy evolution and failure characteristics of fractured rock under uniaxial cyclic loading. Sci. Rep. 13, 2678.
Zhu, H., Tang, X., Song, Y., Li, K., Xiao, J., Dusseault, M.B., McLennan, J.D., 2021. An infill well fracturing model and its microseismic events barrier effect: a case in Fuling shale gas reservoir. SPE J 26, 113–134.
Zhukov, V.S., Kuzmin, YuO., 2020. The influence of fracturing of the rocks and model materials on P-Wave propagation velocity: experimental studies. Izvestiya Phys. Solid Earth 56 (4), 470–480.
Zuo, J.-P., Wei, X., Shi, Y., Liu, C., Li, M., Wong, R.H.C., 2020. Experimental study of the ultrasonic and mechanical properties of a naturally fractured limestone. Int. J. Rock Mech. Min. Sci. 125, 104162.

Elisa Mammoliti has a strong background in structural geology, which she applies extensively in hydrogeology and geomechanics. As an experienced geological surveyor, she combines fieldwork with advanced laboratory and non-destructive testing techniques, including ultrasonic spectroscopy and hardness testing (Equotip, Schmidt hammer), to analyze rock properties, fracture networks, and deformation processes. Her research focuses mostly on carbonate rocks, integrating structural and hydrogeological data to understand groundwater flow, rock-water interactions, and mechanical behavior. Elisa employs experimental, numerical, and statistical methods, including machine learning, to improve predictions of rock strength and failure. Her work supports seismic hazard assessment, underground mining, water resource management, and cultural heritage preservation through non-invasive diagnostics. With multiple publications and international collaborations, Elisa's interdisciplinary expertise bridges structural geology, hydrogeology, and geomechanics to address complex geological and engineering challenges.